JOURNAL OF MAGNETIC RESONANCE **134,** 331–349 (1998)
ARTICLE NO. MN981522

Calibration of STUD+ Parameters to Achieve Optimally Efficient Broadband Adiabatic Decoupling in a Single Transient

M. Robin Bendall* and Thomas E. Skinner†

*The Russell Grimwade School of Biochemistry and Molecular Biology, University of Melbourne, Parkville 3052, Victoria, Australia; and †Department of Physics, Wright State University, Dayton, Ohio 45435

Received December 8, 1997; revised May 26, 1998

To provide the most efficient conditions for spin decoupling with least RF power, master calibration curves are provided for the maximum centerband amplitude, and the minimum amplitude for the largest cycling sideband, resulting from STUD+ adiabatic decoupling applied during a single free induction decay. The principal curve is defined as a function of the four most critical experimental input parameters: the maximum amplitude of the RF field, RF_{max}, the length of the sech/tanh pulse, T_p, the extent of the frequency sweep, *bwdth,* and the coupling constant, J_o. Less critical parameters, the effective (or actual) decoupled bandwidth, bw_{eff}, and the sech/tanh truncation factor, β, which become more important as *bwdth* is decreased, are calibrated in separate curves. The relative importance of nine additional factors in determining optimal decoupling performance in a single transient are considered. Specific parameters for efficient adiabatic decoupling can be determined via a set of four equations which will be most useful for ^{13}C decoupling, covering the range of one-bond $^{13}C^{1}H$ coupling constants from 125 to 225 Hz, and decoupled bandwidths of 7 to 100 kHz, with a bandwidth of 100 kHz being the requirement for a 2 GHz spectrometer. The four equations are derived from a recent vector model of adiabatic decoupling, and experiment, supported by computer simulations. The vector model predicts an inverse linear relation between the centerband and maximum sideband amplitudes, and it predicts a simple parabolic relationship between maximum sideband amplitude and the product J_oT_p. The ratio $bwdth/(RF_{max})^2$ can be viewed as a characteristic time scale, τ_c, affecting sideband levels, with $\tau_c \approx T_p$ giving the most efficient STUD+ decoupling, as suggested by the adiabatic condition. Functional relationships between *bwdth* and less critical parameters, bw_{eff} and β, for efficient decoupling can be derived from Bloch-equation calculations of the inversion profile for a single sech/tanh pulse. Residual splitting of the centerband, normally associated with incomplete or inefficient decoupling, is not seen in sech/tanh decoupling and therefore cannot be used as a measure of adiabatic decoupling efficiency. The calibrated experimental performance levels achieved in this study are within 20% of theoretical performance levels derived previously for ideal sech/tanh decoupling at high power, indicating a small scope for further improvement at practical RF power levels. The optimization procedures employed here will be generally applicable to any good combination of adiabatic inversion pulse and phase cycle.

Key Words: **STUD+; broadband decoupling; adiabatic decoupling; hyperbolic secant pulse; sech/tanh pulse.**

INTRODUCTION

Broadband adiabatic decoupling has been shown to be more efficient than composite-pulse decoupling, in terms of average power deposition for large bandwidths (*1*), but the former is characterized by many adjustable parameters. The goal of this study is to make the application of adiabatic decoupling easy and transparent for any bandwidth within a reasonable experimental range by calibrating all variables required for the most efficient decoupling at the lowest level of RF power. Although adiabatic pulses are insensitive to RF miscalibration, providing accurate spin inversion over a large range of RF power levels, the minimization of decoupling power, and thus sample heating, is considered important for applications to valuable heat-sensitive samples such as ^{13}C-labelled proteins. While the procedures adopted here are generally applicable to any range of J, and any adiabatic decoupling scheme, the detail of this article is restricted to broadband ^{13}C ($125 \text{ Hz} < J < 225 \text{ Hz}$) sech/tanh decoupling.

This work is the culmination of two foundation studies: An investigation of cycling sidebands based on a large number of experimental observations with some supporting theory (*2*), and a theoretical vector model of adiabatic decoupling at the high power limit with supporting experiments (*3*), published in this issue. We now extend that research by performing computer simulations and experimental measurements of sideband and centerband amplitudes over a more extensive range of decoupling parameters than was used previously, employing the more recent phase-cycled adiabatic decoupling scheme STUD + (4). The net result is a set of calibration curves and explicit equations for determining decoupling parameters that provide optimal performance under practical experimental conditions, as opposed to theoretical results derived for idealized conditions.

In common with previous descriptions (*1–3*) of sech/tanh (or hyperbolic secant) (*5*) pulses, the sech amplitude modulation and tanh frequency sweep can be written as

$$B_1 = RF_{max}\text{sech } \beta(1 - 2t/T_p), \qquad [1]$$

1090-7807/98 $25.00

and

$$\Delta H = (bwdth/2)\tanh\,\beta(1 - 2t/T_p + s). \qquad [2]$$

A value $\beta = 5.3$ is typically chosen to truncate the exponential decay of the sech function at a value of 0.01, and s is the resonance offset of the pulse in units of $bwdth/2$ where $s = 0$ denotes on-resonance decoupling. A minimum requirement for the user is to know the values of the maximum amplitude of the RF field, RF_{max}, the length of the sech/tanh pulse, T_p, and the extent of the frequency sweep, $\pm bwdth/2$, for most efficient decoupling for a chosen decoupled bandwidth and coupling constant, J_o.

While these four values are the most critical, we consider a further eleven factors which are important in adiabatic decoupling. We begin this work by constraining most of the parameters by practical considerations. We then consider analytical expressions, derived from the vector model of adiabatic decoupling (*3*), which characterize the performance of sech/tanh decoupling both on and off resonance under ideal conditions of high power. We show that these expressions are applicable to on-resonance decoupling at lower RF power required for the most efficient conditions, where phase cycles are used to compensate for non-idealities in the inversion pulses, thus yielding an objective standard and providing simple linear or parabolic relationships between the maximum sideband amplitude, *MSB*, the centerband amplitude, *CB*, and the four critical variables. Finally, by extending these relationships as far as possible off resonance, we determine the effective, or actual useable, decoupled bandwidth, bw_{eff}, which is closely related to *bwdth* and can be defined by criteria based on *MSB* and *CB*. A straightforward relationship between β and *bwdth* is also demonstrated. This strategy achieves the overall goals of the study, producing the most efficient parameters for general broadband decoupling.

VARIABLES IN ADIABATIC DECOUPLING

The prime consideration for any NMR experimentalist, when presented with a new technique, is to quickly ascertain the most efficient conditions for its implementation. Broadband adiabatic decoupling is a formidable challenge since it is characterized by a number of variables: The required quality of the decoupled spectrum; the degree of sample heating; the pulse sequence preceding decoupling; the form of the adiabatic inversion pulse; the number of increments within the pulse waveform; the pulse phase cycle; the length of the free induction decay; the number of NMR transients required for optimum performance; RF inhomogeneity; *bwdth*; the frequency offset, *s*; bw_{eff}; RF_{max} (or the related average RF power); T_p; and J_o. We also define $b_{/RF^2} = bwdth/(RF_{max})^2$, which appears frequently in the analysis below.

Our task in recommending conditions for efficient decoupling is to obtain a sufficient understanding of the effect of each variable so that we do not inadvertently arrive at a false efficiency maximum wildly different from the true maximum, a pitfall of multi-variate problems (field shimming is an example of a multi-variate problem familiar to practicing spectroscopists). Appropriate settings for some parameters can be chosen at the outset, and it is possible to leave optimization of the least sensitive variables to a later stage, permitting the study to focus on the most critical factors. Given the complex interplay of a large number of variables, progress toward optimal decoupling performance is necessarily an iterative process (like field shimming). After three years of developmental work by the authors, this process has both an historical and a logical basis, including trial-and-error experimentation, serendipitous observations, experiments designed on the basis of theoretical models such as the vector model, and computer simulations.

Performance Criteria

While the quality of the decoupled spectrum is a dependent variable, it is necessary to choose a criterion of decoupling performance in advance of optimization, and decide on a reliable means of measuring this quantity. In our first detailed study of the experimental calibration of adiabatic decoupling, we focused on the measurement of cycling sidebands (*2*). We found that sidebands can be measured reproducibly to an accuracy of better than 0.1% relative to the centerband height, *CB*. While we proposed several standards (*2*), the maximum sideband amplitude, *MSB*, across the effective decoupled bandwidth can be easily determined using a computer macro, and we now suggest that the *MSB* is a true reflection of decoupling efficiency. In part this derives from the even distribution of sidebands across the effective bandwidth for sech/tanh decoupling so that an increase in *MSB* reflects a general increase, and any method which reduces the maximum sideband will tend to reduce all sidebands. Conversely, application of a procedure which reduces sidebands across only a portion of the effective bandwidth will not reduce the *MSB* unless one accepts a reduction in the effective bandwidth—a hypothetical method of this type would be less useful than methods which reduce the *MSB* over the full decoupled bandwidth. For the experimentalist, the size of the maximum sideband is a critical issue because of the need to distinguish between the real spectrum, including minor chemical impurities, and spurious resonances.

Other criteria, such as the amplitude or width of the centerband may seem more directly relevant to decoupling, but they cannot be measured experimentally with the same accuracy as *MSB* levels, and so do not lend themselves readily to an evolutionary improvement of decoupling performance. The width of a resonance cannot be measured accurately to two significant figures, and both the amplitude and width of the centerband are subject to variable experimental factors such as field shimming. In contrast, since we measure *MSB* relative to

CB, a relative *MSB* criterion is independent of natural linewidth. In a later section we will show that a calibration curve based on sideband amplitudes can be converted to a calibration curve for centerband amplitudes via computer simulations, with much greater accuracy than can be achieved by measuring *CB* experimentally. This permits us to convert the relative experimental *MSB* measurements to absolute values. We will also show that for adiabatic decoupling, centerband linewidths are constant across a frequency width that actually exceeds the effective bandwidth, although the central peak height decreases with decreasing decoupling efficiency, and so linewidths cannot be used as a measure of decoupling efficiency.

In terms of performance criteria, a common standard is to require *CB* to be greater than 80% of its maxium across the effective decoupled bandwidth. For previous studies using STUD, we used the limit of a 5% *MSB*, which corresponds to 80% CB. For the improved phase cycles employed in STUD+, a limit of 80% for *CB* produces *MSB* levels of about 3.5% or less. We expect that in some applications, maximum sidebands as low as 0.5% may be needed, so for this dependent *MSB* variable we will concentrate on the range 0.5 to 3.5%.

Sample Heating

The amount of sample heating that occurs during decoupling is also a dependent variable, primarily determined by the average decoupling power which is proportional to $(RF_{max})^2$. While the cooling efficiency within the NMR probe is also important, the guideline in relation to this variable is straightforward—the average RF power delivered to the sample should be kept to a minimum. This is the major goal in optimizing decoupling schemes. Sample heating can mask the effectiveness of a decoupling scheme by changing the shim parameters for best spectral resolution. Characterization of the decoupling scheme by the measurement of relative sideband amplitudes, rather than amplitude or width of the centerband, avoids this ambiguity.

The Pulse Sequence Preceding Decoupling

This variable factor provides a good example of the difficulties that can arise when a critical issue has been overlooked. As described in detail elsewhere (*3, 6*), when decoupling the I spins in an IS spin system, the existence of anti-phase S magnetization just prior to decoupling can lead to additional signals which we have dubbed "coherence sidebands." This problem was not recognized prior to the work of Ref. (*2*) and, in consequence, the resulting calibration curves overestimated the sidebands. Fortunately this did not change the major conclusions of that study. However, differences in results obtained at 600 MHz compared to 500 MHz suggested RF inhomogeneity, whereas the real cause was differences in the level of coherence sidebands. In the present study care has been taken to ensure that the preparation pulse sequence is ideal so that no coherence sidebands are generated. Solutions to the general problem of eliminating coherence sidebands in a single transient have been published (*6*).

The Adiabatic Inversion Pulse

A central tenet of composite-pulse decoupling, introduced by Freeman and co-workers (*7*), is that the quality of decoupling depends in the first instance on the quality of the constituent inversion pulses. The same principle can be inferred from the vector model, as presented in Ref. (*3*), Fig. 1a–1c. If the first inversion is not perfect, the S spins are not refocused at the end of T_p, some S signal is lost, and the next pulse in the decoupling sequence must attempt to refocus the S spins—that represents the first possible opportunity for departure from ideality.

We have based our work on the sech/tanh (*5*) pulse because, in terms of percentage inversion across the bandwidth at fixed values of average RF power, this well-known adiabatic pulse has not been improved upon. It easily outperforms the constant/linear (CHIRP), constant/tan, and sin/cos adiabatic pulses (*8*), and the more recent WURST-*n* pulses (*9*) with linear frequency sweeps, as demonstrated previously (*2, 10*). For example, the sech/tanh inversion pulse has an effective bandwidth of at least 47.5 kHz when $bwdth = 50$ kHz, thus limiting any possible improvement to a few percentage points. The choice of adiabatic pulse, discussed further under Conclusions, as an alternative to the sech/tanh pulse can be safely ignored until the more critical parameters are optimized.

In the interim, in choosing the sech/tanh pulse, we will characterize the performance of yet another variable, the point at which the sech and tanh sweeps are truncated. Traditionally, the amplitude modulation is truncated at the 1% level, when $\mathrm{sech}(\beta) = 0.01$ ($\beta = 5.3$). However, we have previously determined (*4*) that optimization of this truncation point can only increase the effective bandwidth by a few percentage points, so this variable can also be left to the final stages of optimization.

The Number of Increments within the Pulse Waveform

In usual experimental practice, the adiabatic pulse waveforms are digitized in n_i increments, and this results in a decoupled bandwidth which is repeated at frequencies centered on $\pm n_i/T_p$. To prevent these profiles overlapping the central decoupled profile, it was noted in Ref. (*2*) that n_i must be significantly greater than $T_p\ bwdth$. In the course of the many detailed measurements made for this study, it was found that measurable reductions in *MSB* could be observed by increasing n_i until it was greater than $2.5T_p\ bwdth$ and this is the minimum standard now applied.

The Phase Cycle

The choice of phase cycle poses a problem which has many solutions, and it is probably impossible to claim that the

ultimate cycle has been determined. However, there are some realistic approaches to this question. While some specific phase cycling algorithms (*4, 7, 11, 12*) have been used to improve decoupling performance, no general algorithm has been proposed that assures optimal decoupling efficiency. In consequence, we found it necessary to resort to an informed trial-and-error approach in determining the 112-phase cycle of STUD+. More than 40 different phase cycles were tested using the *MSB* criterion and of these the eight best phase cycles are listed in Table 1 of Ref. (*4*) with a progression to lower *MSB* for longer phase cycles.

It will be difficult to greatly improve on these cycles. There are diminishing returns in introducing longer cycles as these cycles become a large fraction of T_2^*, or of the length of the line-broadened S-spin FID. Table 1 of Ref. (*4*) shows a 45% reduction in *MSB* going from the basic 20-phase cycle (*13*) of STUD to a 56-phase cycle (*14*). However, the 112-phase cycle of STUD+ provides only a further 12% reduction. Later in this paper we will show that the STUD+ scheme is most efficient under conditions where it exhibits an overall 60% reduction in *MSB* compared to STUD. Under the same conditions, a further 10% reduction in *MSB* would be equivalent to ideal decoupling in the high power limit where the phase cycle has no effect, and no further reduction is possible.

The Length of the Free Induction Decay

This semi-independent variable can affect the characterization and optimization of a decoupling scheme because of a potential conflict with the product of T_p and the number of phases in the decoupling cycle. If that product is greater than the length of the FID, or greater than the signal acquisition time, then part of the phase cycle for the decoupling scheme has no effect. In this study we have avoided the problem by ensuring that the acquisition time (0.5 s) and the FID (approximately 2 Hz natural linewidth, line-broadened to 3.5 Hz at half height) are significantly longer than this product. Commonly, FIDs are a fraction of a second so this aspect reinforces the expectation of diminishing improvements from longer phase cycles.

The Number of Transients Required for Optimal Performance

Our approach to this variable is straightforward. We define it as an independent variable and set the number at one transient. There are two important reasons for doing so. First, determining the most efficient conditions for minimizing the *MSB* in one transient ensures that the *CB* is maximum and thus overall *S*/*N* is maximum. Methods which reduce sidebands via interference resulting from changed parameters between transients do not increase the centerband while averaging sideband intensity to smaller values. Second, in 3D and 4D NMR it is often necessary to reduce the number of transients for each increment to provide adequate resolution within a reasonable total acquisition time. For this reason, pulsed-field gradients have become popular as an alternative to phase cycling. If possible, spin decoupling schemes should not increase the overall number of transients required for each multi-dimensional increment.

If, having determined the optimum conditions for decoupling, it is found that sidebands need to be further suppressed in particular applications, multi-transient methods such as the accordion technique (variation of T_p) of Starcuk *et al.* (*15*), which performs well over the full decoupled bandwidth, can then be employed. In passing we note that standard multi-transient methods of reducing sidebands do not always work with adiabatic decoupling as exemplified by the illustration of asynchronous decoupling in Ref. (*3*).

RF Inhomogeneity

All pulse sequences are subject to potential variation of the RF field across the sensitive volume of the sample, but we see no effects from adiabatic decoupling that can be ascribed to RF inhomogeneity. In particular, we obtain close agreement between theoretical simulations, which assume no RF inhomogeneity, and experiment. There are two independent explanations for this. First, modern RF probes have high homogeneity and the excellent characteristics of the probe used for this work are listed under Experimental. Furthermore, because the sensitive volumes for S (^{1}H) and I (^{13}C) are closely matched, the boundaries of the overall volume are sharp because the profile of the *S*/*N* response across the sample is a product of the individual profiles for each RF pulse. Second, plots of sideband amplitude versus decreasing RF field strength for adiabatic decoupling (e.g., as in Fig. 1) show a rather slow rate of increase in sideband amplitude in the regions where decoupling is most efficient. Thus a 10% variation say, in RF across the sample, will give almost identical sideband levels to those yielded by a single value of RF field strength. Experimental RF calibrations provide such single values as averages across the sensitive volume, and so we are able to ignore the potential problem of RF inhomogeneity in this study.

Bandwidth (bwdth), Effective Bandwidth (bw_{eff}), and Frequency Offset (s)

The *bwdth* parameter is a critical independent variable. From previous work (*3, 4*), for sech/tanh decoupling, maximum sidebands show a flat response across a wide range of frequency offset (dimensionless parameter, *s*) which ultimately determines the effective bandwidth, bw_{eff}. We will seek the most efficient conditions for STUD+ by concentrating on this region of flat response, and then determine bw_{eff}. For broadband sech/tanh decoupling, this is a reasonable procedure because the effective bandwidth is already known to be a large fraction of *bwdth*, and can be maximized after other critical variables are addressed.

The Most Critical Variables, bwdth, RF_{max}, T_p, and J_o

These four parameters remain as critical independent variables but are also constrained in important ways. In terms of present magnetic field strengths, and future developments, we are primarily concerned with broadband decoupling in the 10 to 100 kHz range. Maximum RF field strengths are limited to about 20 kHz in high resolution NMR but we have found this sufficient to decouple bandwidths exceeding 500 kHz using sech/tanh decoupling (*10*). Limiting the *MSB* to 3.5% sets the maximum T_p at 2.5 ms for ^{13}C decoupling, and J_o is known to be 125–225 Hz for ^{13}C.

EXPERIMENTAL

Proton-detected ^{13}C-decoupled spectra were obtained as in previous studies (*1, 3, 6*) following a heteronuclear spin-echo difference pulse sequence using a standard 5-mm HCN triple-resonance PFG probe on a 500-MHz Varian INOVA spectrometer. Three samples were employed: 1.5% $^{13}CH_3CO_2Na$ in D_2O, doped with sufficient $MnCl_2$ to produce a coupled linewidth of 2.2 Hz, J_o = 127 Hz; 2% $^{13}CH_3I$ in $CDCl_3$, doped with 0.2% $Cr(AcAc)_3$ relaxation agent, coupled linewidth = 1.7 Hz, J_o = 150 Hz; and 2% of the isopropyl ester of $H^{13}CO_2H$ in $CDCl_3$, doped with 0.2% $Cr(AcAc)_3$ relaxation agent, coupled linewidth = 2.0 Hz, J_o = 223 Hz. Exponential line broadening was applied to FIDs of 0.5-s duration to produce coupled linewidths of 3.5 Hz. Equal field gradient pulses were employed either side of the refocusing pulse in the spin-echo pulse sequence to eliminate artifact signals, and the overall $1/J_o$ spin-echo delay time was set exactly with respect to each of the above J_o values.

RF amplitudes were calibrated by determining the 180° on-resonance pulse time for ^{13}C, and are expressed as the reciprocal of the 360° pulse time in units of hertz. A total of 16 calibrations over a range from 11.5 kHz down to 1.9 kHz were made at each of 1dB increments of coarse attenuator by varying the RF amplitude and length of a single 90° ^{13}C pulse in a DEPT-HMQC sequence to obtain a 180° null. It was ascertained that the same calibration could be obtained (with less accuracy) by changing the 180° ^{13}C pulse in the spin-echo difference sequence to 360° to obtain a *S*/*N* null. Decoupling measurements were made with RF_{max} determined by these 1-dB settings and the RF calibration was checked at at least one of these settings before and after each group of measurements. Matched values of T_p giving the best decoupling performance as a function of $bwdth/(RF_{max})^2$ in Eqs. [3], [7], or [8], were rounded to the nearest 0.1 ms.

RF inhomogeneity of single ^{1}H and ^{13}C pulses for the NMR probe is characterized by a *S*/*N* loss of 24% when a 90° ^{1}H pulse is increased to 810°, and a loss of 33% when a ^{13}C θ pulse is set at 720° in a ^{1}H-detected experiment which yields zero signal when θ = 90°—the sensitive volume in the sample relevant to the decoupling measurements is determined by the product of the sensitive volumes from each of the three pulses in the preparatory spin-echo sequence, so the effect of RF inhomogeneity is much reduced compared to these figures.

Sideband amplitudes were measured at *bwdth* values of 10, 50, and 100 kHz with the sech/tanh pulses digitized in 250 increments for 10 kHz, and 500 increments for the 50 and 100 kHz settings. In each spectrum the peak heights of the centerband and the four major sidebands at $1/(mT_p)$, m = 1, 2, 5, 10, were measured after baseline correction using a spline fit (standard Varian NMR software). The largest sideband amplitude, divided by the centerband amplitude, *CB*, was recorded as the relative *MSB* amplitude (i.e., as a relative percentage of *CB*). For on-resonance measurements, eight transients were acquired for each spectrum.

For off-resonance decoupling two transients were acquired for each spectrum. For *bwdth* values of 10 and 50 kHz, spectra were obtained at frequency offsets incremented by 100 Hz from zero offset to $bwdth/2$. For *bwdth* = 100 kHz, the increments were 200 Hz. It was determined by experimentation that the effective bandwidth of decoupling at the same average RF power was maximized by setting the truncation factor, β, of the constituent sech/tanh pulses to 3.1 at *bwdth* = 10 kHz, 4.3 at *bwdth* = 50 kHz, and 5.0 at *bwdth* = 100 kHz. The same average power was maintained by varying the fine RF power linear attenuator in proportion to $(\beta/5.3)^{0.5}$ while maintaining the coarse RF power attenuator at the value calibrated for RF_{max}. Measurements of centerband linewidth at half height were made at *bwdth* = 50 kHz, J_o = 223 Hz, β = 5.3, RF_{max} = 6.2 kHz, T_p = 1.3 ms in increments of 500 Hz from zero offset. Two transients with an acquisition time of 2 s were obtained for each spectrum subsequent to two dummy transients, and a minimum delay of one minute was included between each measurement—without this delay, additional line broadening from sample heating occurred after about ten measurements.

The computer simulations were obtained for the case of a single carbon coupled to a single proton detected on resonance using a standard density matrix calculation of the detected signal, as outlined in Ref. (*16*). The Bloch equations were solved as a function of time using a fourth-order Runge–Kutta algorithm with adaptive stepsize control for the sech/tanh driving functions of Eqs. [1]–[2] and the STUD+ phase cycle, with ΔH modified to include the coupling offsets $\pm J_o/2$. The total resonance offset is thus $\Delta H(t) \pm J_o/2$, depending on whether the attached spins are aligned with the $\pm z$ axis. The Euler angles of the rotated coordinate axes were determined for offset ($s + J_o/bwdth$) as a function of time and used to derive the equivalent single rotation in SU(2) at each time. The procedure was repeated for offset ($s - J_o/bwdth$) and the parameters of the equivalent rotations were used to construct the time-domain signal given by Eq. [60] in Ref. (*16*), which was Fourier transformed to determine centerband and sideband amplitudes. Alternatively, the acquisition time can be divided into subintervals of equal length, sufficiently small to ensure

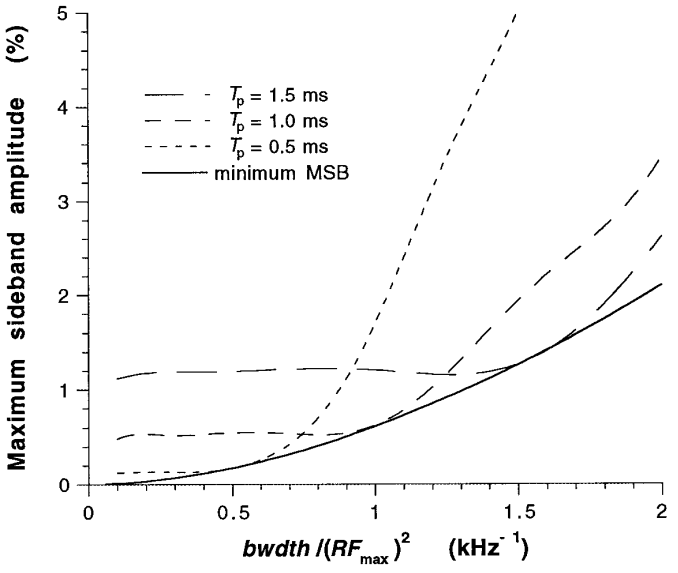

FIG. 1. Simulations of STUD+ decoupling on resonance ($s = 0$) at constant $bwdth = 50$ kHz and $J_o = 150$ Hz were performed as functions of the experimental input parameters T_p and the ratio $b_{/RF^2} = bwdth/(RF_{max})^2$. T_p was varied over the range 0.1–3.0 ms in increments of 0.1 ms, while $b_{/RF^2}$ was similarly incremented by 0.1 kHz^{-1} over the range 0.1–3.0 kHz^{-1}. Results for the amplitude of the maximum sideband (*MSB*) are plotted as a function of $b_{/RF^2}$ for a subset of the thirty T_p values in increments of 0.5 ms. *MSB* amplitudes are expressed as a percentage of the centerband (*CB*) amplitude. Similar results are obtained for *bwdth* in the range 20–100 kHz, since, as shown in Ref. (*2*), *MSB* at a given T_p depends on $b_{/RF^2}$ and is relatively insensitive to the particular value of *bwdth*. The underlying envelope of the curves shows that for a given value of $b_{/RF^2}$, there is a corresponding value for T_p that minimizes the *MSB* amplitude and yields the most efficient decoupling. This is illustrated further in an alternative plot of *MSB* as a function of T_p for fixed b/RF^2 in Fig. 5, where the simulations are performed over the full decoupled bandwidth.

the Hamiltonian, and, hence, the time evolution operator, is effectively constant during each subinterval. The SU(2) parameters at each time are obtained directly by concatenating the appropriate sequence of successive evolution operators. Approximately 85,000 spectra were simulated and analyzed with the results summarized in Figs. 1–5. The accuracy of the simulations has been demonstrated previously (*3*) by the correspondence between them, vector model calculations, and experiment. The simulated signals in Fig. 2 were generated using only eight samples per inversion pulse, resulting in a slight underestimate of the *MSB* for some points, but this does not affect the conclusions for Fig. 2. Peak heights in the simulations are accurately rendered for sampling rates greater than 16 per inversion, and all other simulations were performed using 64 samples per inversion pulse.

These simulations, further described in the captions to Figs. 1 and 5, produce absolute (*ABS*) *MSB* and centerband amplitudes, and relative (*REL*) *MSB* amplitudes are given by $REL = ABS/CB$. A plot of absolute *MSB* amplitudes versus relative *MSB* amplitudes for the minimum *MSB* values (at matched T_p and $bwdth/(RF_{max})^2$ values given by Eq. [3]) obtained from simulations of on-resonance decoupling yields the relation $ABS = 0.98*REL - 0.047*REL^2$ ($R^2 = 0.99997$) where both *ABS* and *REL* are in percent. This relationship was used to convert the relative experimental measurements to absolute prior to plotting in Figs. 2 and 4. Similarly, the minimum *MSB* and corresponding *CB* determined by simulations off resonance yields $ABS = 0.98*REL - 0.040*REL^2$ ($R^2 = 0.99995$). This was used to convert the Fig. 8 experimental data to absolute measurements.

Both simulated and experimental data were curve fitted using KaleidaGraph (Abelbeck Software). This procedure used a Levenberg–Marquardt non-linear least squares algorithm which minimizes χ^2. The goodness-of-fit is listed as R^2 which is the square of Pearson's r and is related to χ^2 by $R^2 = 1 - \chi^2/(\Sigma\{y_i - y_m\}^2)$ where y_i = actual value, and y_m = mean of actual values.

CALIBRATION CURVE FOR ON-RESONANCE (s = 0) STUD+ DECOUPLING

The primary optimization strategy for broadband decoupling is to minimize sample heating (RF power) for a chosen level of decoupling performance (*bwdth* and *MSB*), or, equivalently, to minimize the *MSB* at constant *bwdth* and RF_{max}. The major goal is to obtain a master calibration curve which corresponds to these optimum conditions and provides values of T_p and RF_{max} for any chosen set of *bwdth*, *MSB*, and J_o.

Part of this task was achieved in Ref. (*2*), where we showed experimentally and theoretically for STUD that for any *bwdth* value between 10 and 100 kHz, the same dependence of *MSB* on $bwdth/(RF_{max})^2$ is obtained at constant T_p, with separate curves obtained at different T_p values. The same behavior is obtained for STUD+, and with coherence sidebands now understood and eliminated, there is a close agreement between *MSB* levels at the same value of $bwdth/(RF_{max})^2$ at constant T_p for all bandwidths in the range we are currently most interested in, 10 to 100 kHz. This universal dependence on $bwdth/(RF_{max})^2$ is shown by other adiabatic schemes, and will remain a constant feature throughout this paper, so this term has been abbreviated to $b_{/RF^2}$.

Simulations of *MSB* levels versus $b_{/RF^2}$ at constant T_p for the on-resonance case ($s = 0$) are shown in Fig. 1 for a coupling constant $J_0 = 150$ Hz. These have the same form as the experimental curves of Ref. (*2*), which were obtained over the full decoupled bandwidth. Both sets of curves show that, at any value of $b_{/RF^2}$, there is a corresponding value of T_p which gives a minimum *MSB* value indicated by the points where the individual curves touch the underlying envelope illustrated in Fig. 1. For example, at $T_p = 1.0$ ms, a minimum *MSB* on resonance of ~0.5% is achieved at $b_{/RF^2} \approx 1.0$ for $J_0 = 150$ Hz, and both shorter and longer values of T_p increase the *MSB* levels relative to the envelope. Plots of *MSB* versus T_p at incremented $b_{/RF^2}$ will pass through minima corresponding to the same points and can be used to determine the relation between T_p and $b_{/RF^2}$ that gives the most efficient decoupling. A later figure for off-resonance decoupling, Fig. 5, is illustra-

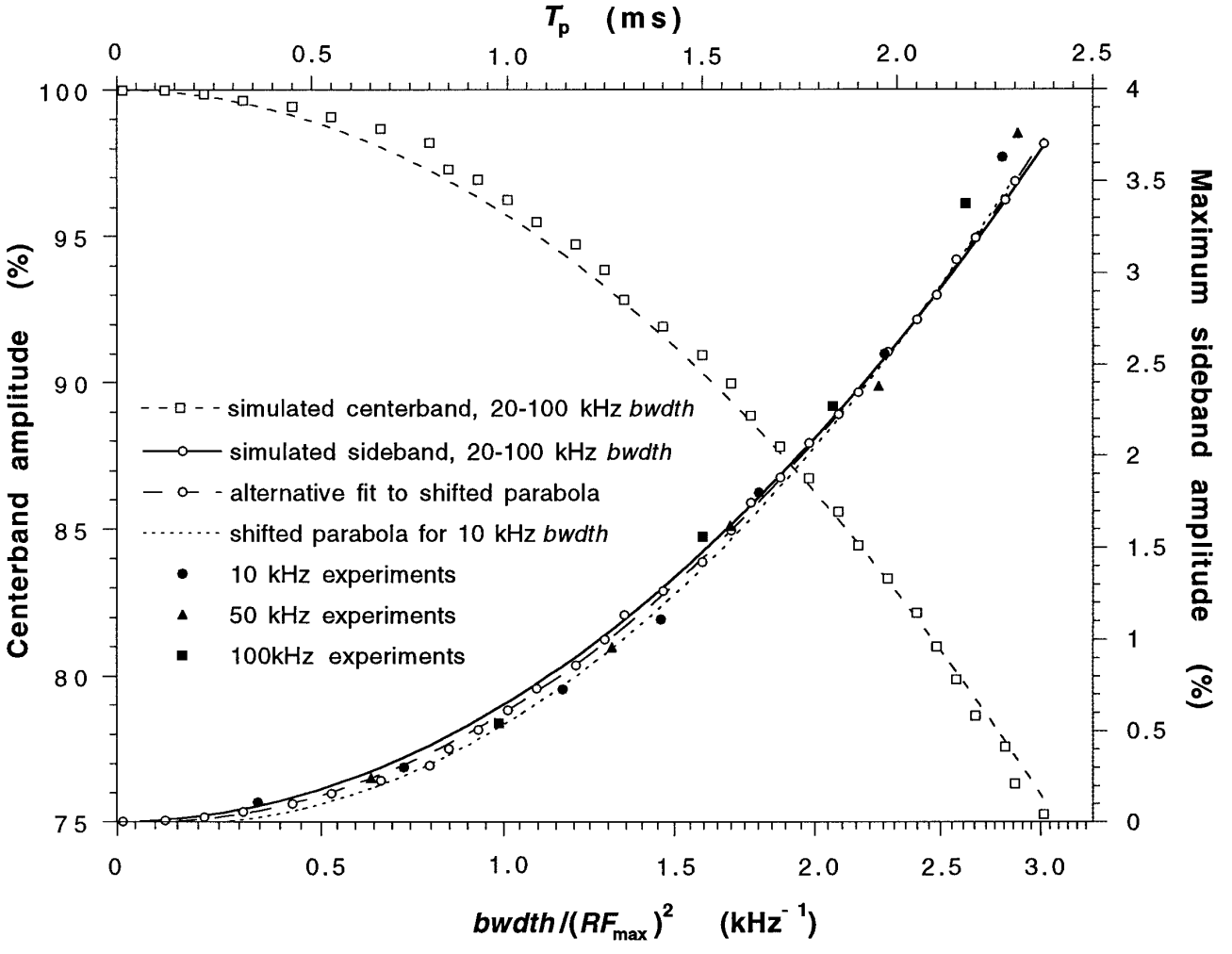

FIG. 2. Matched values of $b_{/RF^2}$ and T_p that produce the minimum *MSB* and the maximum centerband amplitude (*CB*) were determined from the simulations illustrated in Fig. 1. The maximum *CB* (open squares, left axis) and minimum *MSB* (open circles, right axis) are plotted as functions of the matched pairs, $b_{/RF^2}$ (bottom axis) and T_p (top axis), for STUD+ decoupling applied on resonance ($s = 0$) for $J_o = 150$ Hz. The unfilled points are the average of computer simulations of minimum *MSB* and corresponding maximum *CB* levels at *bwdth* values of 20, 50, and 100 kHz. The T_p and $b_{/RF^2}$ axes are related by Eq. [3]. The solid curve fitted to the simulated *MSB* data is a simple parabola (vertex at the origin) corresponding to Eq. [5] ($R^2 = 0.9990$), and the alternative dashed curve is a parabola (vertex is shifted from the origin) given by $MSB = -0.085T_p + 0.70T_p^2$ ($R^2 = 0.9996$). The parabolic curve fitted to the simulated centerband (*CB*) data is $CB = 100 - 4.3T_p^2$ ($R^2 = 0.997$) and, as noted in the text, the *CB* data is related to the *MSB* data by $CB = 100 - 6.57*MSB$. Simulated *MSB* results (not shown) were also plotted for *bwdth* = 10 kHz and fitted to a second shifted parabola as $MSB = -0.21T_p + 0.76T_p^2$ ($R^2 = 0.996$). The experimental *MSB* data (solid points) were obtained with a $^{13}CH_3I$ sample ($J_o = 150$ Hz) and on-resonance STUD+ decoupling, at matched values of $b_{/RF^2}$ and T_p given by Eq. [3] and at *bwdth* values of 10, 50, and 100 kHz. The experimental data were measured relative to the centerband and have been converted to absolute percentages as described under Experimental.

tive of this procedure, although the minima obtained off resonance are broader and exhibit more irregularities than the minima obtained on resonance.

The minimum *MSB* was obtained as a function of T_p, which was varied between 0.1 and 3.0 ms for each $b_{/RF^2}$ in the range 0.1 to 3.0 kHz^{-1} using computer simulations at *bwdth* values of 20, 50, and 100 kHz. Since the experimental dependence of *MSB* on $b_{/RF^2}$ has been shown to be insensitive to *bwdth* (*2*), the minimum *MSB* as a function of T_p for fixed $b_{/RF^2}$ occurred at the same value of T_p (± 0.1 ms) for each of these three *bwdth* values, as expected. Figure 2 shows the calibration curve obtained, by averaging the three sets of results, for the minimum *MSB* plotted as functions of the matched values, $b_{/RF^2}$ and T_p, that give the most efficient decoupling performance under on-resonance conditions. Good agreement was obtained with experiment, as is also shown in the figure. Experimental *MSB* levels obtained with unmatched $b_{/RF^2}$ and T_p were found to be displaced from the curve of optimal performance by increasing amounts as the difference between T_p and its optimal value for a given $b_{/RF^2}$ was increased, in accordance with the theoretical curves illustrated in Fig. 1. The relationship between T_p (ms) and

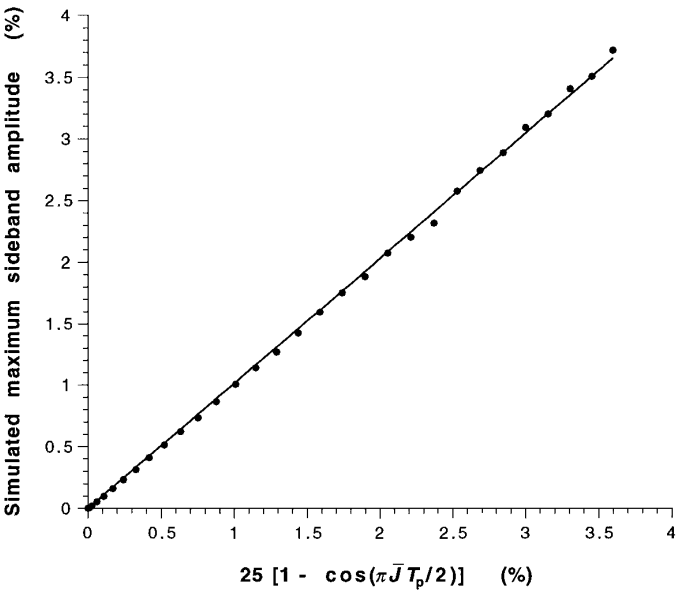

FIG. 3. Simulated minimum *MSB* amplitudes expressed as a percentage of the centerband amplitude, calculated as described in the legend to Fig. 2 (averaged for *bwdth* values of 20, 50, and 100 kHz), are plotted against the function $0.25[1 - \cos(\pi\bar{J}T_p/2)]$ (for *bwdth* = 50 kHz, and also expressed as a percentage), where $\bar{J}$ is the average coupling constant during half a sech/tanh pulse calculated as described in Refs. (*3*) or (*8*) at the $b_{/RF^2}$ values used in the simulations. The data points fit a straight line through the origin with slope = 1.014 ($R^2 = 0.9994$).

$b_{/RF^2}$ (kHz^{-1}) for most efficient decoupling, as determined from the simulations, is

$$T_p = (1.11 - 0.11b_{/RF^2})(b_{/RF^2}), \qquad [3]$$

and both the T_p and $b_{/RF^2}$ scales are provided in Fig. 2.

It was of interest to investigate whether this calibration curve could be related back to the vector model of Ref. (*3*). In that study it was shown that in the limit of high RF decoupling power ($b_{/RF^2} \leq 0.5$ kHz^{-1}), the *MSB* occurred at $1/T_p$, with smaller harmonics at n/T_p, and analytical expressions giving the amplitude of these sidebands were derived. A rough estimate of the $1/T_p$ sideband is given by $0.25[1 - \cos(\pi\bar{J}T_p/2)]$, which is half the maximum amplitude of the modulation of the S-spin FID in the limit of high RF power. This maximum occurs at the middle of each sech/tanh decoupling pulse and $\bar{J}$ is the average coupling constant during half a sech/tanh pulse. Figure 3 shows a plot of the average *MSB* results obtained from the computer simulations shown in Fig. 2 versus $0.25[1 - \cos(\pi\bar{J}T_p/2)]$ for *bwdth* = 50 kHz. $\bar{J}$ was calculated as described in the Fig. 3 legend. The plot is a straight line of unit slope and zero intercept, illustrating a strong correlation between the optimal performance values determined from simulation and experiment, and the ideal performance that can be obtained in the high-power limit. However, the slope of unity is serendipitous. In Ref. (*3*) it was demonstrated that the $1/T_p$ sideband is given by the Fourier transform of the vector-model S-spin signal, $\cos(\pi J_o \alpha(t) T_p/2)$, where $\alpha(t)$ is an analytical expression depending on RF_{max}, β, T_p, and *bwdth*. This exact result for the amplitude of the $1/T_p$ sideband at $b_{/RF^2} = 0.1$ kHz^{-1} is less than the estimate given by $0.25[1 - \cos(\pi\bar{J}T_p/2)]$ by a factor $k_1 = 0.73$, and this factor is constant for all T_p in the range 0.1 to 3 ms. As described earlier in the discussion pertaining to Fig. 1, the most efficient decoupling conditions for a given T_p occur at values of $b_{/RF^2}$ where the individual curve intersects the envelope of the curves. Here, the *MSB* is some small factor k_2 greater than the $1/T_p$ sideband produced in the high power limit at lower values of $b_{/RF^2}$. This occurs at points where the $1/(5T_p)$ sideband (or another $1/(mT_p)$ sideband where $m > 2$) has increased until it exceeds the $1/T_p$ sideband by the same k_2 factor. A comparsion of minimum MSB values for a given $b_{/RF^2}$, plotted in Fig. 2, with the corresponding high-power limit values for MSB at the same T_p in Fig. 1 show that $k_2 = 1.37$ so that $k_1 k_2 \approx 1$.

This correspondence with the vector model is useful in several ways. First, it again justifies the utility of the model as one which describes decoupling in the high power limit and we then attempt to mimic this ideal case by using phase cycling schemes.

Second, for on-resonance conditions at least, it provides an easy means via the function, $0.25[1 - \cos(\pi\bar{J}T_p/2)]$, of determining the *MSB* for most efficient decoupling at a particular T_p.

Third, except for a weak dependence of $\bar{J}$ on *bwdth* and RF_{max}, these latter parameters are not included in the function, $0.25[1 - \cos(\pi\bar{J}T_p/2)]$, and this implies they do not significantly affect the quality of decoupling once the matched conditions imposed by Eq. [3] are realised. $\bar{J}$, the average coupling constant during half a sech/tanh pulse, can be calculated as described in Refs. (*3*) or (*8*). It ranges modestly as $0.88J_o$, $0.91J_o$, and $0.95J_o$ for *bwdth* values of 10, 20, and 100 kHz at $b_{/RF^2} = 0.5$ kHz^{-1} to just $0.94J_o$, $0.95J_o$, and $0.98J_o$, respectively at $b_{/RF^2} = 2.5$ kHz^{-1}. There is a corresponding minor divergence of the simulated *MSB* amplitudes for *bwdth* = 10 kHz away from the averaged simulated data for *bwdth* values of 20, 50, and 100 kHz, which increases at lower $b_{/RF^2}$, as illustrated by the two shifted-parabola fits to the data shown in Fig. 2. The experimental results in the Figs. 2, 4, and 8 also indicate slightly lower *MSB* values for a 10-kHz bandwidth.

Fourth, ignoring the weak dependence of $\bar{J}$ on *bwdth* and RF_{max}, since $(1 - \cos x)$ is proportional to x^2 for small x,

$$MSB = 0.25k_1k_2[1 - \cos(\pi\bar{J}T_p/2)] = k_3T_p^2. \qquad [4]$$

This justifies the excellent fit of the experimental and simulated data to the solid curve in Fig. 2, which is a simple parabola (vertex at the origin) given by

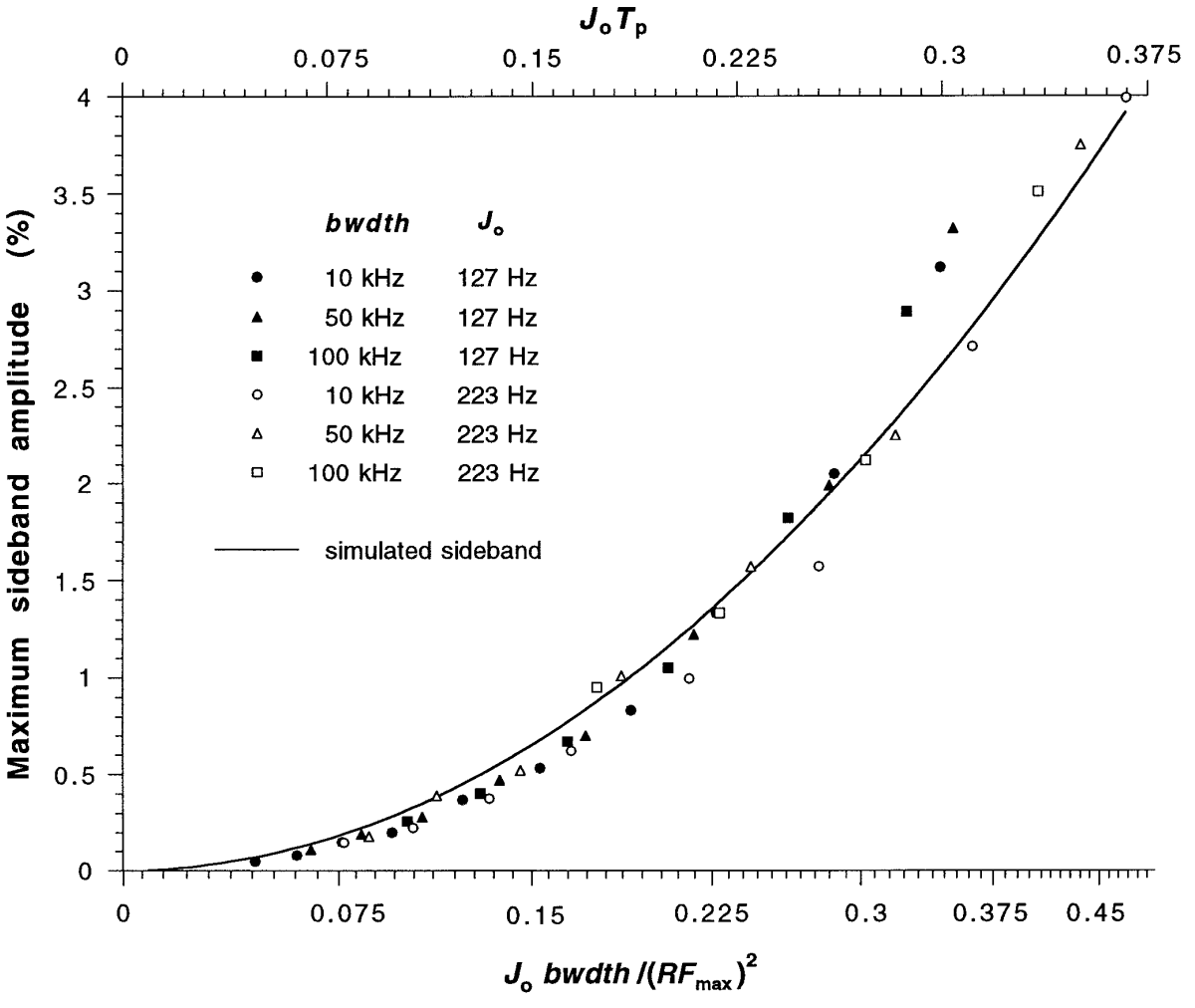

FIG. 4. Similar to Fig. 2, but the effect of changing the coupling constant is considered. Experimental values of minimum *MSB* measured using a $^{13}CH_3CO_2Na$ (J_o = 127 Hz) sample and a $H^{13}CO_2H$ (J_o = 223 Hz) ester sample, as a result of on-resonance STUD+ decoupling at matched values of $b_{/RF^2}$ and T_p from Fig. 2 and at *bwdth* values of 10, 50, and 100 kHz, are plotted against J_oT_p and $J_ob_{/RF^2}$. The top and bottom axes are related by Eq. [3] and have been rescaled by J_o according to the discussion surrounding Eq. [6]. The *x*-axes are dimensionless. The solid curve, which is fitted to simulated *MSB* data (not shown), is the same as the solid curve in Fig. 2, illustrating there is a simple relationship that determines the optimal choice of $b_{/RF^2}$ and T_p and minimizes the *MSB* (i.e., most efficient decoupling) for on-resonance STUD+ decoupling over a range of J_0 values appropriate to $^{13}C^1H_n$ systems. Extensions to the full decoupled bandwidth of STUD+ are considered in subsequent figures.

$$MSB = 0.654T_p^2, \qquad [5]$$

where *MSB* is in percent of the centerband, and T_p is in milliseconds. The simulated sidebands and experimental points plotted in Fig. 2 demonstrate a slight tendency towards a general quadratic (parabola with vertex shifted from the origin), rather than Eq. [5], resulting from the approximations implicit in the above discussion. In addition the experimental points at high $b_{/RF^2}$ show a small displacement towards higher *MSB* than the simulated results, which we ascribe to experimental artifact or error. These deviations are small and ultimately cannot be seen in the off-resonance results discussed in the next section.

Fifth, the centerband amplitude is proportional to the amplitude of the S-spin FID with the decoupling modulation subtracted. Since $0.25[1 - \cos(\pi\bar{J}T_p/2)]$ is half the maximum amplitude of the modulation of the S-spin FID in the limit of ideal decoupling at low $b_{/RF^2}$, under those conditions the decrease in the centerband is proportional to this function. This is confirmed by the linear relation between the *MSB* and *CB* data at high RF power which can be derived from the vector-model results in Ref. (*3*). We now find that the form of these relations extends to the data at lower RF power or higher *bwdth* in Fig. 2. There is a close linear correspondence between simulated *MSB* and *CB*, with *CB* (%) decreasing as a function of increasing *MSB* (%) according to the relation $100 - CB = 6.57*MSB$ ($R^2 = 0.998$), and the fit of the *CB* data, an inverted parabola compared to the *MSB* data, is illustrated in

the figure. This numerical correspondence between *CB* and *MSB* supports our emphasis on quantifying *MSB* levels to provide an accurate measure of decoupling performance.

Sixth, $\bar{J} = J_o\alpha(T_p/2)$ in Eq. [4] indicates how decoupling performance might be related to J_o. Again ignoring the weak dependence of $\bar{J}$ on *bwdth* and RF_{max}, the function, $0.25[1 - \cos(\pi\bar{J}T_p/2)]$, is also proportional to J_o^2, since the argument of the cosine is small. Thus different J_o values might be accommodated by rescaling the dependent *MSB* axis of the calibration curve by $(J_o/150)^2$, or by converting the *x*-axis to either $J_o b_{/RF^2}$ or $J_o T_p$ as in Fig. 4, and one can write

$$MSB = k(J_o T_p)^2 = 29.1(J_o T_p)^2, \qquad [6]$$

where *MSB* is in percent of the centerband, J_o is in Hz, and T_p is in seconds, giving $k_3 = k(150/1000)^2$ in Eq. [4]. The experimental results for $J_o = 127$ and 223 Hz in Fig. 4 show the same minor tendency (as in Fig. 2) towards a shifted parabola rather than the simple parabolic curve of Eqs. [4]–[6] resulting from higher order terms in the expansion of the cosine. However, the overall excellent correspondence between this simple theory and experiment indicates that we can relate the *MSB* and *CB*, for on-resonance sech/tanh decoupling at the most efficient RF power, back to the function $0.25k_1k_2[1 - \cos(\pi\bar{J}T_p/2)]$ for a range of J_o values appropriate to $^{13}C^1H_n$ systems.

We conclude that the single calibration curve for *MSB* amplitude, and the associated curve for centerband amplitude, in Figs. 2 or 4, suffice to provide values of the parameters RF_{max} and T_p for any chosen values of *bwdth* and J_o for STUD+ ^{13}C decoupling under the most efficient conditions on resonance. Individual experimental data points correspond to the analytical expressions derived from computer simulations and basic theory (the vector model) and thus prove these equations without any inherent subjectivity. We next proceed to demonstrate the more general validity of this analysis for off-resonance decoupling, but the determination of effective bandwidths is wholly experimental and thus partly subjective.

MASTER CALIBRATION CURVES FOR STUD+ DECOUPLING

The vector model of adiabatic decoupling (*3*) demonstrates that for ideal decoupling (e.g., $b_{/RF^2} \leq 0.5T_p$), the *MSB* on resonance was the $1/T_p$ sideband. The harmonics at n/T_p are smaller and higher-order sidebands at $1/(mT_p)$ are zero under ideal adiabatic conditions on resonance. The $1/(mT_p)$ sidebands remain less than the $1/T_p$ sideband far off resonance, but for I spins having frequencies near the extremes of the frequency sweep ($s \approx \pm 1$) the adiabatic condition is violated and one or more of the $1/(mT_p)$ sidebands rapidly increases above the level of the on-resonance $1/T_p$ sideband as the limits, $s = \pm 1$, are approached. Thus, in terms of sidebands, for sech/tanh decoupling, there is a region of flat response across a large fraction of *bwdth* and this matches a near constant centerband amplitude. Accordingly, a good definition of the effective bandwidth in the high power limit is the fraction of *bwdth* within which the *MSB* is the on-resonance $1/T_p$ sideband.

The on-resonance simulations and experiments at lower power, as described in the previous section, show that the most efficient conditions, in terms of minimum *MSB* at a given average power, occur when one of the $1/(mT_p)$ sidebands has grown to be 37% larger than the $1/T_p$ sideband ($k_2 = 1.37$ in Eq. [4]). The next question is whether this latter result at most efficient power can be extended off resonance in the same way the simple rules for high-power decoupling were applicable off resonance. Given the relatively constant values of *MSB* as a function of decoupler resonance offset for the sech/tanh functions, we might expect this to be the case within limits determined by some *MSB* criterion that we choose to apply.

Matched Values of T_p and bwdth/$(RF_{max})^2$

Theoretical simulations were conducted for a range of decoupler offsets given by $0 \leq |s| \leq 0.92$ in *s* increments of 0.01 over the same range of variation in $b_{/RF^2}$ and T_p described earlier. The large number of small increments, required to provide confidence that regions of high *MSB* amplitude were not missed, was computationally intensive, so only a single *bwdth* value of 50 kHz at $J_o = 150$ Hz was used for the off-resonance simulations. The results for the *MSB* in this offset range are plotted in Fig. 5 as a function of T_p for fixed values of $b_{/RF^2}$. Only a subset of curves for $b_{/RF^2}$ incremented by 0.5 kHz^{-1} are displayed for clarity in the figure.

For the on-resonance case, the *MSB* minima were well enough defined to readily provide the most efficient T_p value within 0.1 ms, yielding Eq. [3]. But the curves in Fig. 5 are broader near the minimum *MSB* than for the on-resonance case, with the T_p value corresponding to the lowest *MSB* shifting somewhat erratically from one curve at fixed $b_{/RF^2}$ to the next. One approach is to assume that the variations across the relatively broad minima will change with *bwdth*, and that the overall centers of the broad minima represent the best estimates of the most efficient decoupling conditions. Repetition of the simulations at several *bwdth* values (and averaging the results), as for the on-resonance procedure, would be unnecessarily time consuming so these centers were estimated as the midpoint between points on the outside wings of the broad minima where the *MSB* level had risen 7% or more above the lowest *MSB* for each $b_{/RF^2}$ value. A plot of T_p (ms) matched to $b_{/RF^2}$ (kHz^{-1}) in this way provided the curve ($R^2 = 0.992$)

$$T_p = (1.40 - 0.17b_{/RF^2})(b_{/RF^2}). \qquad [7]$$

A replot of the *MSB* amplitude for the matched conditions of Eq. [7] versus the estimate of the $1/T_p$ sideband given by the function, $0.25[1 - \cos(\pi\bar{J}T_p/2)]$, yielded a reasonably straight line ($R^2 = 0.992$; slope = 1), and so the calibration curve could be represented by a simple parabola, as for the on-

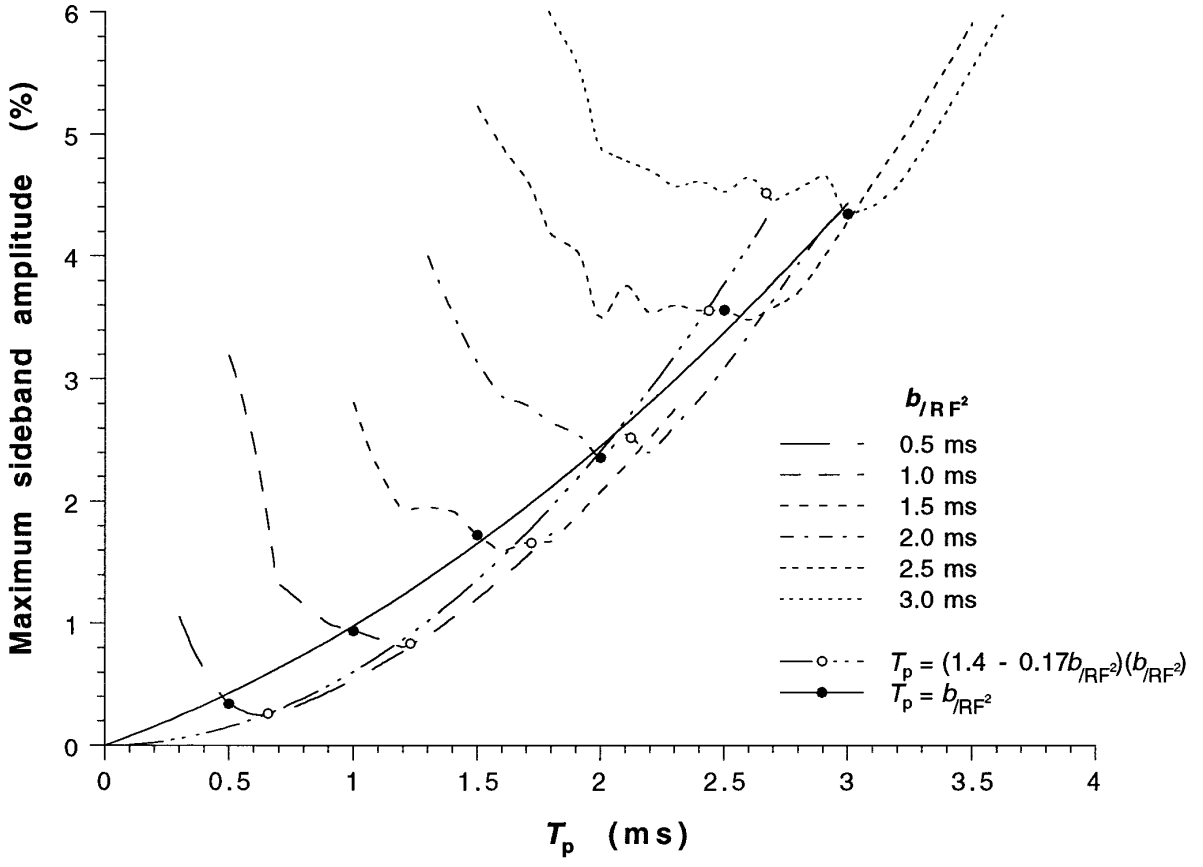

FIG. 5. Simulations were performed for the same experimental input parameters and over the same range of variation in $b_{/RF^2}$ and T_p as described in the legend to Fig. 1, except the *MSB* level was determined over a frequency offset range of $0 \leq s \leq 0.92$, incrementing s by 0.01 (for $b_{/RF^2} = 0.5$ kHz^{-1}, $0 \leq s \leq 0.90$ to accurately reflect the decrease in effective decoupled bandwidth at lower values of *bwdth*). Simulated *MSB* amplitudes are plotted as a function of T_p for a subset of the 30 $b_{/RF^2}$ values in increments of 0.5 kHz^{-1}. Individual simulated values of *MSB* for fixed $b_{/RF^2}$ (not shown) have been connected by interpolating curve fits. The unfilled points correspond to *MSB* levels at the midpoint of the relatively broad neighborhood surrounding the minimum *MSB*. These matched values of T_p and $b_{/RF^2}$ are given by Eq. [7]. The filled points (and solid curve) represent *MSB* levels for matched values given by the simpler relation $T_p = b_{/RF^2}$, which leads to slight improvements in the effective decoupled bandwidth in some cases and is therefore preferred to Eq. [7]. Details are provided in the text.

resonance case. Very good agreement was obtained between theory and experiment for these matched T_p and $b_{/RF^2}$ conditions, similar to the on-resonance results in Fig. 2.

Our investigative plan as expressed above was to first concentrate on the region of flat response across a large fraction of *bwdth* ($0 \leq |s| \leq 0.92$) as in Fig. 5, and then optimize the effective bandwidth. Because the simulated data of Fig. 5 will sustain a range of equations differing from Eq. [7], it is possible that the region of flat response might be extended by some other match between T_p and $b_{/RF^2}$. Accordingly, T_p was incremented in steps of 0.1 ms for five different values of $b_{/RF^2}$ for each of *bwdth* = 10, 50, and 100 kHz. Via direct experimental comparisons, *MSB* levels decreased by up to 20% at the edge of the bandwidth, or remained the same, when T_p was changed from the value given by Eq. [7] to

$$T_p = b_{/RF^2}. \qquad [8]$$

Across the normal range of T_p, Eq. [8] does not differ greatly from Eq. [7], as shown in Fig. 5, and increases in the effective bandwidth were only a maximum of 3% for *bwdth* = 50 kHz, and even more modest at 10 kHz and 100 kHz. But however small the gains, Eq. [8] has the advantage and the additional complexity of Eq. [7] cannot be justified.

Effective Bandwidth (bw_{eff})

The experimental estimation of the limit of bw_{eff} is initially partly subjective. In some cases, with increasing $|s|$, the *MSB* amplitude increases rapidly and smoothly at the edge of the bandwidth and there is little difference between determining the limit as the point where the *MSB* had increased 10%, or increased 20%. In other cases the *MSB* rises 10–20% near the edge of the effective bandwidth before decreasing and then increasing more rapidly. Thus the choice of whether a 10% or a 20% increase is acceptable becomes more critical. But an

objective procedure is not as simple as allowing, say, an increase of 10%, because the question immediately arises as to what constitutes the base sideband level against which the increase should be compared. For example, if the base level is chosen to be the *MSB* amplitude across 90% of the bw_{eff}, this base number will vary erratically by a few percent as demonstrated by the simulations in Fig. 5, and so the "objective" standard will also be erratic. Considering that our overall goal was to fit a large number of experimental points to smooth calibration curves it was decided that this source of variance would eventually be averaged out by the scatter of points either side of the final curve. Generally a temporary rise of up to 20% in *MSB* near the edge of the effective bandwidth was considered acceptable, but in cases where the *MSB* showed a continuous rapid increase, the limit was set at 15% above the preceding flat region.

As mentioned above, another variable that can have a small but worthwhile effect is the point at which the sech and tanh sweeps are truncated, traditionally set at a 1% cutoff where $\text{sech}^{-1}(0.01) = 5.3$. Experimental determination of bw_{eff} by increasing the truncation level, i.e., decreasing the β factor of 5.3, has a beneficial effect at lower *bwdth* values. At *bwdth* = 10 kHz, the effective bandwidth is increased by up to 6% of *bwdth* when the truncation cutoff is increased to 9%. These measurements were made at constant average RF power by multiplying the value of $RF_{\max}$ used for $\beta = 5.3$ by $(\beta/5.3)^{0.5}$, where β is the new truncation factor. A calibration curve of truncation level versus $(bwdth)^{-1}$ is provided in Fig. 6. This optimization of sech/tanh truncation leads to modest improvements in bw_{eff} at low bandwidths, but does not change the overall *MSB* amplitude. Thus, the experimental points shown later in Fig. 8 were obtained with optimized truncation factors, but are plotted at the equivalent $b_{/\text{RF}^2}$ value where $RF_{\max}$ corresponds to the traditional β factor of 5.3, so that we can continue to employ a common calibration curve for all *bwdth* values. Alternatively, to avoid any confusion, a scale for *bwdth* divided by (average power) is also provided in Fig. 8.

Plots of effective bandwidth, expressed as a fraction in percent, f_s, of *bwdth*, versus *bwdth*, obtained using the optimized truncation factors of Fig. 6, are shown in Fig. 7. These differ from the previous Fig. 7 of Ref. (*2*) to show minor dependencies on the chosen *MSB* level, and on J_o, which were revealed by the present more detailed study. All data sets can be easily fitted to smooth curves by observing that there is a linear relationship between bw_{eff} and *bwdth*. Expressing this in an inverse manner with bw_{eff} as the independent variable, to permit the calculation of *bwdth* from a chosen effective bandwidth,

$$bwdth = m_1 + m_2 bw_{\text{eff}}. \qquad [9]$$

The intercepts, m_1, and slopes, m_2, are listed in Fig. 7. Plots of

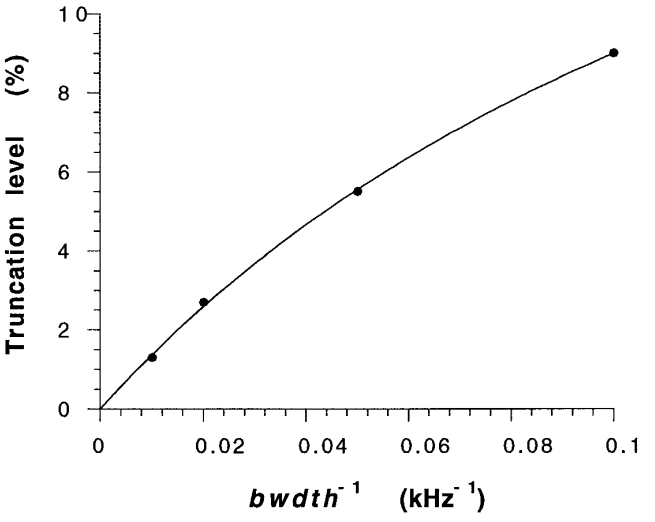

FIG. 6. Experimentally determined optimum truncation levels (TL), for the hyperbolic secant amplitude modulation function plotted against reciprocal *bwdth*, which provide maximum effective bandwidths for STUD+ decoupling when using a $^{13}CH_3I$ sample (J_o = 150 Hz). The standard for determining the effective decoupled bandwidth is discussed in detail under *Effective Bandwidth.* The data have been fitted to a curve given by $TL = 23.5(1 + 0.161bwdth)^{-1}$ ($R = 0.9997$). The truncation level is related to the truncation factor, β, by $TL = 100 \text{ sech } \beta$.

these straight lines are very similar and do not readily convey the dependence on chosen *MSB* and J_o. These minor differences are magnified by the plots in Fig. 7 where

$$f_s = 100bw_{\text{eff}}/bwdth = 100(1 - m_1/bwdth)/m_2. \qquad [10]$$

The linear relationships expressed in Eq. [9] were not anticipated in Ref. (*2*). While it might be argued that a three-point data set is too small to permit a definitive conclusion of linearity, there are five such data sets in Fig. 7 and each set yielded a goodness-of-fit R^2 value greater than 0.99997. Data points at other *bwdth* values can be obtained, but each is the result of the analysis of at least 150 spectra, and the accuracy of the results in Fig. 7 is sufficient for the calibration of decoupling parameters for routine application.

In the prior study (Fig. 7 of Ref. (*2*)), we obtained a smooth curve to fit the experimental data by relating bw_{eff} to the effective bandwidth for inversion by a single sech/tanh pulse. The new procedure encapsulated by Eqs. [9] and [10] is simpler and more direct. The two approaches are reconciled by observing that the effective bandwidth for inversion is also governed by Eqs. [9] or [10]. This can be rapidly established with a very high degree of accuracy, because for a single pulse it is easy to generate inversion profiles (in the absence of *J* coupling and at constant $b_{/\text{RF}^2} = T_p$) by Bloch-equation calculations, and obtain many simulated data points at different *bwdth* values. For large *bwdth*, sech/tanh pulses yield, almost ideal, square inversion profiles, with a slight rounding of the

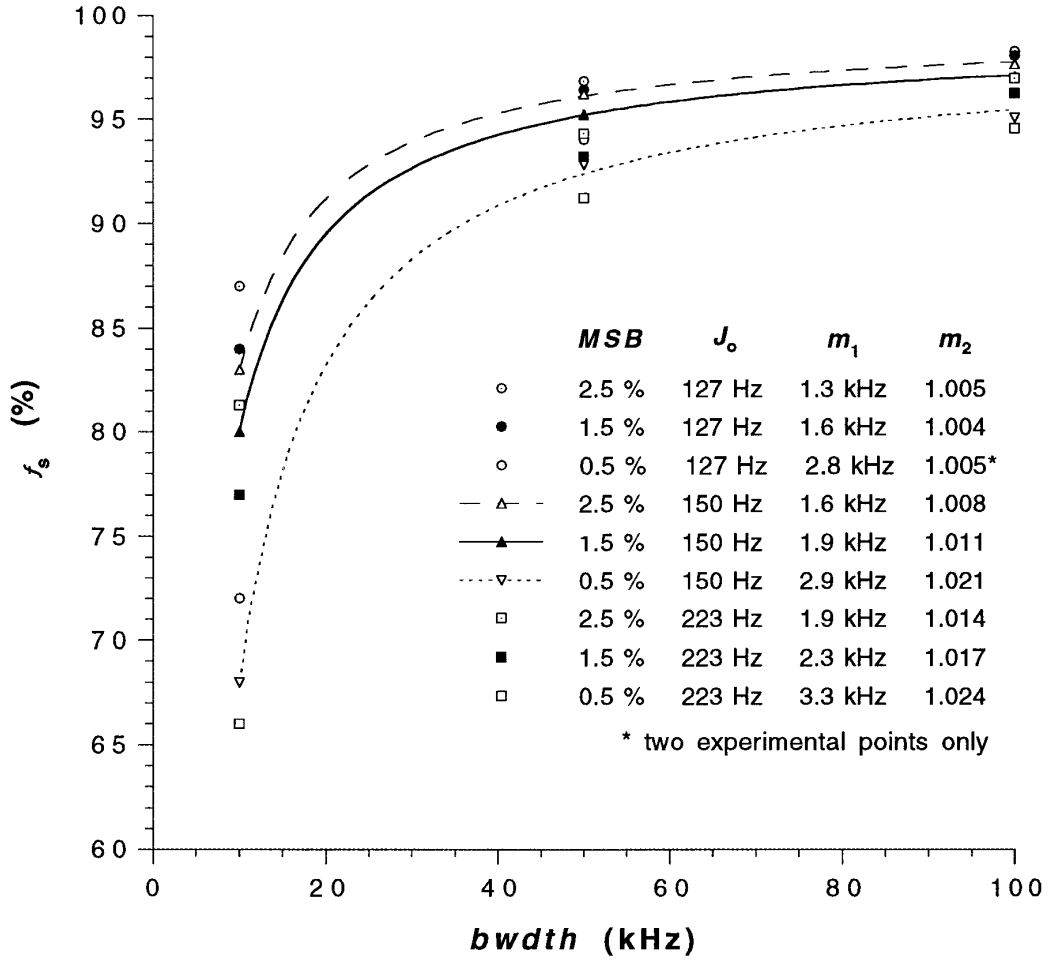

FIG. 7. The ratio f_s (of bw_{eff} in percent of *bwdth*) plotted versus *bwdth*. Effective bandwidths, bw_{eff}, were measured at a choice of three different *MSB* levels of 2.5, 1.5, and 0.5% for three different coupling constants of 127, 150, and 223 Hz exhibited by the chemicals $^{13}CH_3CO_2Na$, $^{13}CH_3I$, and $H^{13}CO_2H$ (ester). A set of three experimental points was obtained at *bwdth* values of 10, 50, and 100 kHz for each chosen combination of *MSB* and J_o. Each set of points was fitted to the equation $f_s = 100(1 - m_1/bwdth)/m_2$, which is equivalent to $bwdth = m_1 + m_2 bw_{eff}$, and the intercepts, m_1, and slopes, m_2, of these linear relations are listed in the figure. In each case $R^2 \geq 0.99997$, indicating the sufficiency of the three-point data sets. The m_1 and m_2 values can in turn be fitted to straight lines as $m_1 = 1.3 + 0.8/MSB$ ($R^2 = 0.996$) and $m_2 = 1.005 + 0.008/MSB$ ($R^2 = 0.989$) for $J_o = 150$ Hz; and $m_1 = 1.7 + 0.8/MSB$ ($R^2 = 0.97$) and $m_2 = 1.012 + 0.006/MSB$ ($R^2 = 0.98$) for $J_o = 223$ Hz. To simplify Eq. [18] for determining the experimental input parameter *bwdth* for a desired *MSB* and bw_{eff} at a coupling J_o, this last relation for m_2 was modified to $m_2 = 1.010 + 0.008/MSB$ ($R^2 = 0.92$)—this change is within experimental error and has a trivial effect on the *bwdth* estimates derived from Eq. [18].

corners, as illustrated by Fig. 8 of Ref. (*8*). The effective bandwidth for inversion can be defined by a chosen percentage inversion limit on the profile shoulder. The simulations show that for a constant β truncation factor and a constant inversion limit, bw_{eff} and *bwdth* are related by Eq. [9] with $m_2 = 1$. We have noted (*2*) that the adiabatic condition is proportional to $(b_{/RF^2})/T_p$ so maintenance of a constant ratio between $b_{/RF^2}$ and T_p as in Eq. [8] should maintain some commonality for different *bwdth* values, especially at the middle of inversion profiles. This adiabatic condition also suggests that the squareness of inversion profiles should scale with the dimensionless offset parameter, *s*, and so reduce m_2 below unity. But the detailed Bloch calculations prove via the relation, $bwdth = m_1 + bw_{eff}$, that the reduction in squareness is manifested in m_1 and so the profiles get worse for lower *bwdth*. Thus the shoulders of the inversion profile always have the same shape in terms of absolute frequency units, not dimensionless *s*, under these conditions. This observation, and Eq. [9], no longer apply when *bwdth* is so small that the two mirror-image shoulders begin to meet in the middle of the overall profile, i.e., when *bwdth* is about $2m_1$ or less.

Inclusion of a β truncation factor that varies with *bwdth* (as determined in Fig. 6) in the inversion calculations, changes m_2 from unity to values of the same order as those listed for decoupling in Fig. 7. This variable truncation factor decreases the intercept, m_1, which dominates at low *bwdth*, so increasing bw_{eff} at low *bwdth* while having a negligible effect at high *bwdth*. Thus all aspects of the shape of the decoupling profile

would seem to correlate well with the profile for a single sech/tanh inversion pulse, which accounts for the advantage this pulse enjoys over other adiabatic pulses used for decoupling. Our overall study is limited to $bwdth \geq 10$ kHz to avoid the additional complexity that arises when $bwdth$ is of the same order as $2m_1$. However, we do not find an exact correlation between decoupling and inversion probably because J_o coupling has not been included in the latter. We observe closer correlation, between the m_1 and m_2 values in Fig. 7 and those from inversion calculations, if J_o is added to the m_1 values for the latter. However the experimental decoupling data are both insufficient in number and accuracy to support a definitive conclusion as to this minor effect of J_o on the squareness of the profile shoulders. A precise description of the effect requires a full quantum mechanical calculation but is of such low significance to broadband decoupling that there is little to gain for the present study. Note that most of the increase in m_1 with increasing J_o in Fig. 7 derives from Eq. [11] below, rather than this small effect of J_o on the shape of the inversion profile. Increased J_o requires smaller T_p for the same *MSB* level, and reducing T_p (and $b_{/RF^2}$) reduces the squareness of the profile for both inversion and decoupling.

In comparing effective bandwidths for decoupling to inversion profiles for single pulses, it is of interest that, for example, for the (1.5%, 150 Hz) data set in Fig. 7, a single pulse inverts I_z magnetization to $0.7I_{-z}$ at the center of the profile. This gives an example of the extent to which the STUD+ phase cycle must correct for these poor inversions, so that the average amount of I_z and I_{-z} after each pulse equalizes cyclically during the decoupling scheme.

The data in Fig. 7 demonstrate the small extent to which the effective bandwidth can be improved by using some other form of adiabatic pulse, or some other phase cycle. The only real scope for improvement is the frequency-independent squareness of the inversion profile, i.e., reduction of the m_1 value of about 2 kHz. This will be important in narrowband applications where selectivity is the prime criterion, not average RF power, and alterations to the form of the adiabatic pulse should improve the profile just as we were able to gain modest improvements at $bwdth = 10$ kHz by altering the truncation factor for the sech/tanh pulse.

Experimental Data and the Master Calibration Curve

The overall results are brought together in the optimized master curve data of Fig. 8 which provides *MSB* levels across the effective bandwidths displayed in Fig. 7 (up to 98% of $bwdth$) for $bwdth$ values between 10 and 100 kHz, and J_o between 125 and 225 Hz. The experimental points fit well to a simple parabola (vertex at the origin), which in turn can be related back to the on-resonance Eq. [4] and the function, $0.25[1 - \cos(\pi \bar{J} T_p/2)]$, with these relationships summarized by

$$MSB = 32.0(J_o T_p)^2 = 1.14\{25[1 - \cos(\pi \bar{J} T_p/2)]\}, \quad [11]$$

where *MSB* is in percent of the centerband, J_o is in Hz, and T_p is in seconds.

As for the on-resonance results, $\bar{J}$ in Eq. [11] was calculated for $bwdth = 50$ kHz, which produces an *MSB* plot approximately equidistant between slightly displaced plots for $bwdth = 20$ and 100 kHz. The experimental measurements in Fig. 8 again illustrate the modest trend to lower *MSB* levels for $bwdth = 10$ kHz. There is also a weak trend in Fig. 8 to higher *MSB* levels at higher J_o values than given by the master curve. However, the more significant trend is that an increased J_o results in a smaller effective bandwidth, as discussed in the preceding section concerning Fig. 7, where bw_{eff} is 6% less for $J_o = 223$ than 127 Hz at $bwdth = 10$ kHz, although it is within a 1% difference at $bwdth = 100$ kHz.

While the parabolic fit through the origin in Fig. 8 is very good ($R^2 = 0.960$), it is clear that a parabola with a small y intercept is better ($R^2 = 0.968$) even though such a non-zero intercept has no theoretical justification. The source of this intercept arises from the unavoidable subjectivity involved in experimentally determining the effective bandwidth. From Fig. 7, bw_{eff} decreases with decreasing $b_{/RF^2}$ (smaller *MSB*) and there is a natural subjective bias towards accepting a higher effective bandwidth and a higher minimum *MSB* when determining these limits. Clearly the estimates in both Fig. 7 and Fig. 8 could be reworked, but there can be little or no gain in terms of practical applications where *MSB* levels below 0.5% would rarely be warranted. In any event, the present figures with slightly higher *MSB* and bw_{eff} values at the high power end of the normal RF range are valid experimental calibrations of efficient decoupling. The *y* intercept in Fig. 8 serves as a reminder that the curves are experimental in origin.

A Calibration Curve for Centerband Amplitude

The filled data points in Fig. 5, for which $T_p = b_{/RF^2}$, do not fit a parabolic curve through the origin as well as the experimental data in Fig. 8 because the simulations were obtained over the constant range of $0 \leq s \leq 0.92$ rather than a range that increases with increasing $b_{/RF^2}$ as demonstrated by the experimental data in Fig. 7. The curve for $b_{/RF^2} = 0.5$ kHz^{-1} was recalculated over $0 \leq s \leq 0.90$ for the presentation in Fig. 5 once it was realized that $s = 0.92$ exceeded the effective bandwidth for that case, but in general, minimum *MSB* levels derived from the simulations over $0 \leq s \leq 0.92$ were a little high at low $b_{/RF^2}$ and a little low at high $b_{/RF^2}$ with good correspondence to the experimental measurements for $1 \leq b_{/RF^2} \leq 2$ kHz^{-1}. While the simulations could be repeated to take into account the increase in effective bandwidth with $b_{/RF^2}$, no new information would be gained. The demonstration of a very good fit of the experimental data to a parabola in Fig.

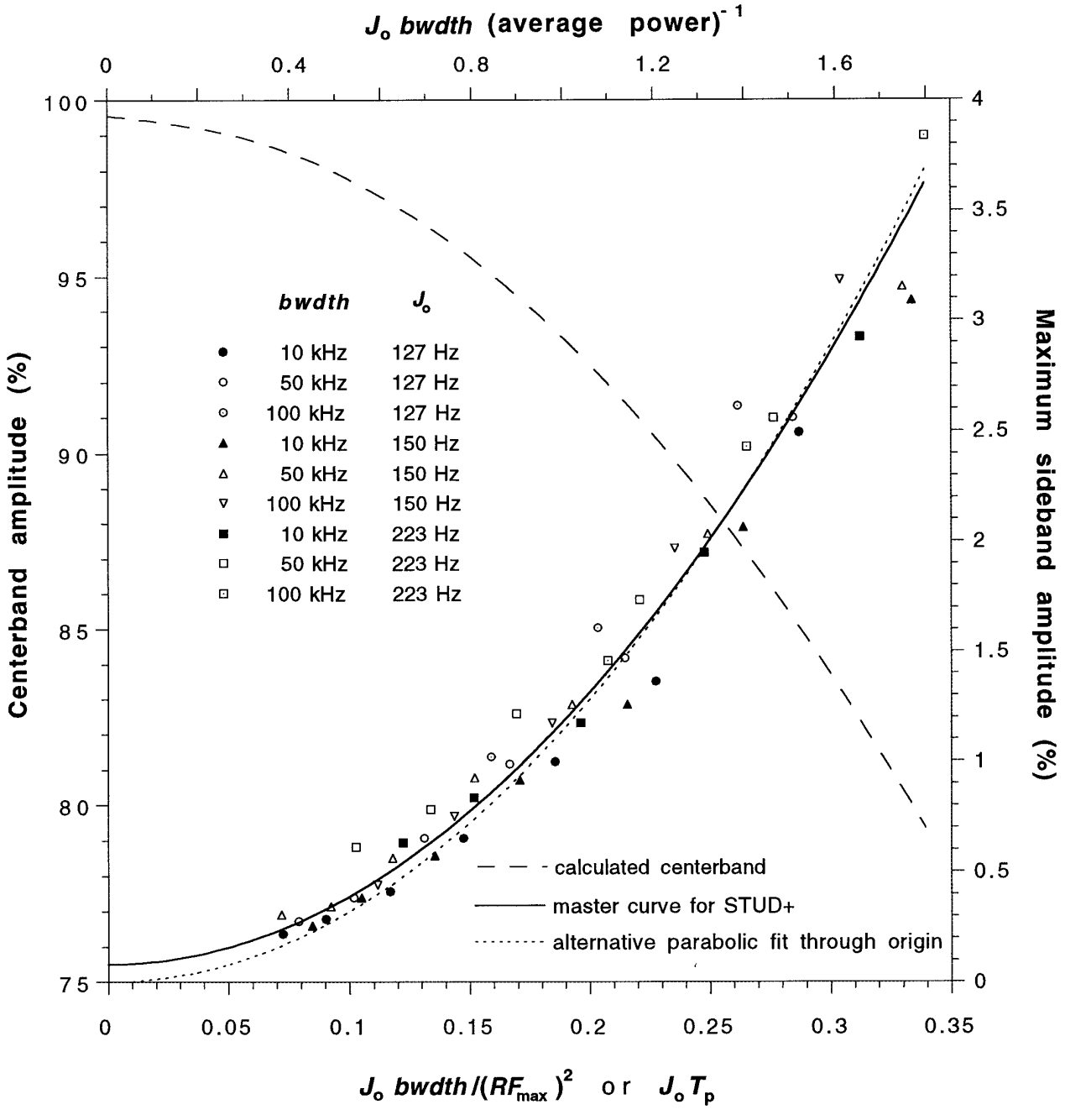

FIG. 8. Master calibration curve (solid line) for the optimal values of the parameters, RF_{max}, *bwdth*, and T_p, that produce the minimum *MSB* at a coupling J_o over an effective decoupled bandwidth, bw_{eff}, equal to f_s times *bwdth* from Fig. 7. The set of equations for determining these optimal values is described under *Practical* ^{13}C *Decoupling Parameters.* Experimental *MSB* levels for STUD+ decoupling across the same effective bandwidths as above are plotted versus $J_oT_p = J_ob_{/RF^2}$, for the three coupling constants of 127, 150, and 223 Hz exhibited by the chemicals $^{13}CH_3CO_2Na$, $^{13}CH_3I$, and $H^{13}CO_2H$ (ester) and values of 10, 50, and 100 kHz for *bwdth.* The sech/tanh pulses comprising the STUD+ scheme utilized a variable truncation factor, β, calibrated in Fig. 6, and an RF_{max} scaled as $(\beta/5.3)^{0.5}$ relative to the RF_{max} at the traditional value of $\beta = 5.3$. Thus the value of $b_{/RF^2}$, represented by the bottom scale of $J_oT_p = J_ob_{/RF^2}$, is for the equivalent average power when $\beta = 5.3$ and the top scale is related to the bottom scale by average power $= (RF_{max})^2/5.3$. The master curve, a parabola, is fitted to the experimental points by $MSB = 0.08 + 30.8(J_oT_p)^2$ ($R^2 = 0.973$), and the alternative simple parabola through the origin (dashed curve) is fitted to $MSB = 32.0\,(J_oT_p)^2$ ($R^2 = 0.968$). The curve for the centerband amplitude is derived from the solid master curve using Eq. [12]. The *x*-axes are dimensionless.

8, in contrast to the limited simulation data, again is evidence that subjectivity has largely been avoided.

However, as noted above, the simulations provide absolute estimates of sidebands and centerbands, whereas accurate experimental data are restricted to the determination of sideband amplitudes relative to centerband amplitudes. As for the on-

resonance data in Fig. 2, the computer results (plotted in part in Fig. 5) show that there is a linear correspondence between minimum *MSB* (%) and maximum *CB* (%) for $T_p = b_{/RF^2}$ yielding the relation

$$100 - CB = 5.7*MSB. \quad [12]$$

For low values of $T_p = b_{/RF^2}$ the values for both the original $0 \le s \le 0.92$ data and the recalculated $0 \le s \le 0.90$ data fit this equation. Given the exactness of Eq. [12] ($R^2 = 0.997$), and the overlap with the experimental data for $0.5 \le b_{/RF^2} \le 2$, the associated relation between relative and absolute measures of sideband amplitudes has been used to convert the relative experimental data to absolute in the plot of *MSB* levels in Fig. 8 (see Experimental). In addition, Eq. [12] has been used to provide a calibration curve in Fig. 8 for the centerband amplitude derived from the experimental *MSB* data.

As mentioned above, one accepted measure of decoupling efficiency is the amount of residual splitting associated with the centerband (*7, 16*). If not resolved, this splitting will be present as line broadening. A careful study was made at low power, $J_o = 223$ Hz, and $bwdth = 50$ kHz, corresponding to a centerband amplitude of 85% on the master curve of Fig. 8 where residual splitting should be greatest. Four-transient spectra were obtained with long delays between each spectrum to ensure that sample heating caused no line broadening. No resolvable splitting of the centerband was observed at any frequency offset, including offsets corresponding to $f_s > 100\%$ where the centerband amplitude rapidly decreases to zero corresponding to the sharp transition to a completely coupled spectrum. Indeed, compared to coupled linewidths, line broadening of only 0.2 to 0.3 Hz was measured across almost the entire 50 kHz frequency sweep, out to $f_s \le 97\%$, which exceeds the effective bandwidth determined in Fig. 7 as $f_s = 91\%$. This confirms that residual splitting, or line broadening, of the centerband does not accurately reflect adiabatic decoupling efficiency, and that it is an insignificant effect compared to normal linewidths.

The Master Curve Compared to Ideal Decoupling

The minimum *MSB* can be directly compared to the magnitude of the $1/T_p$ sideband on resonance, determined from the vector model (*3) for* $T_p = b_{/RF^2}$ using the function, $\cos(\pi J_o \alpha(t) T_p/2)$, as described above in the On-Resonance section. This calculation assumes that the I spins remain aligned with the effective field, B_e, at all times so that only sidebands at n/T_p are generated, which is to say that it is assumed that the adiabatic condition is not violated. Under such theoretical conditions the modulation of the S-spin FID is repeated exactly for every sech/tanh pulse and total sideband intensity is minimized. Experimentally, single-transient methods cannot reduce sidebands below values obtained under these conditions of ideal adiabaticity. The vector model calculations (for T_p increments of 0.1 ms and $J_o = 150$ Hz) were fitted ($R^2 = 0.99994$) to a simple parabola (vertex at the origin) yielding

$$MSB = 24.1(J_o T_p)^2 = 0.86\{25[1 - \cos(\pi \bar{J} T_p/2)]\}. \quad [13]$$

where *MSB* is in percent of the centerband, J_o is in Hz, and T_p is in seconds. This represents the lowest possible *MSB* level at a chosen value of $J_o T_p$ and the curve for these theoretical conditions is plotted as "ideal decoupling" in Fig. 9. The factor of 0.86 is greater than $k_1 = 0.73$ in the On-Resonance section because the latter was for high power conditions ($b_{/RF^2} = 0.1$ kHz^{-1}). Comparing the previous results for STUD to those for STUD+ and to ideal decoupling indicates that the STUD sidebands have been reduced by 58%, and only a further reduction of 11% is possible. But it is arguably more appropriate to compare Eq. [13] with the on-resonance result of Eq. [6], because Eq. [11] includes the nominal 15% *MSB* tolerance in experimentally determining the limits of the effective bandwidth. This comparison indicates that only a further 4% reduction is possible beyond the improvement in going from STUD to STUD+. It is for these reasons that we noted earlier that there is not much potential gain to be had in improving the phase cycle over that of STUD+.

However, while an absolute limit can be imposed on the minimum *MSB* level achievable at a particular $J_o T_p$ (albeit with minor corrections from large changes in J_o and *bwdth*), the relationship between T_p and $b_{/RF^2}$, whether from Eq. [3], [7], or [8], is based entirely on experiment, or computer simulations to mimic experiment. In determining the optimum relationship for STUD+ we cannot state absolutely that some other phase cycle will not be more efficient because we have no illuminating theory to define the relationship between T_p and $b_{/RF^2}$. In these terms, greater efficiency means a larger $b_{/RF^2}$ value for the same *MSB* and T_p, and thus lower average power for the same *bwdth*, *MSB*, and T_p. This is illustrated in Fig. 9 for the experimental on-resonance curve plotted versus $J_o b_{/RF^2}$ compared to the same curve plotted versus $J_o T_p$, demonstrating that a relationship like Eq. [3] will advantageously alter the $b_{/RF^2}$ scale relative to the T_p scale if it is possible to generate a phase cycle that would achieve this result across the same effective bandwidth. However, we have noted (*2*) that minimum adiabaticity occurs at the midpoint of a sech/tanh pulse where adiabaticity is a function of $(b_{/RF^2})/T_p$, supporting a linear relationship like Eq. [8] rather than quadratic Eqs. [3] or [7] for maximum efficiency. We have also noted above that there must necessarily be diminishing returns for phase cycles longer than STUD+.

Practical ^{13}C Decoupling Parameters

Figures 6–9 provide all necessary parameter settings for broadband ^{13}C decoupling for effective bandwidths from 7 to 95 kHz. From this and previous work (*10*), values for band-

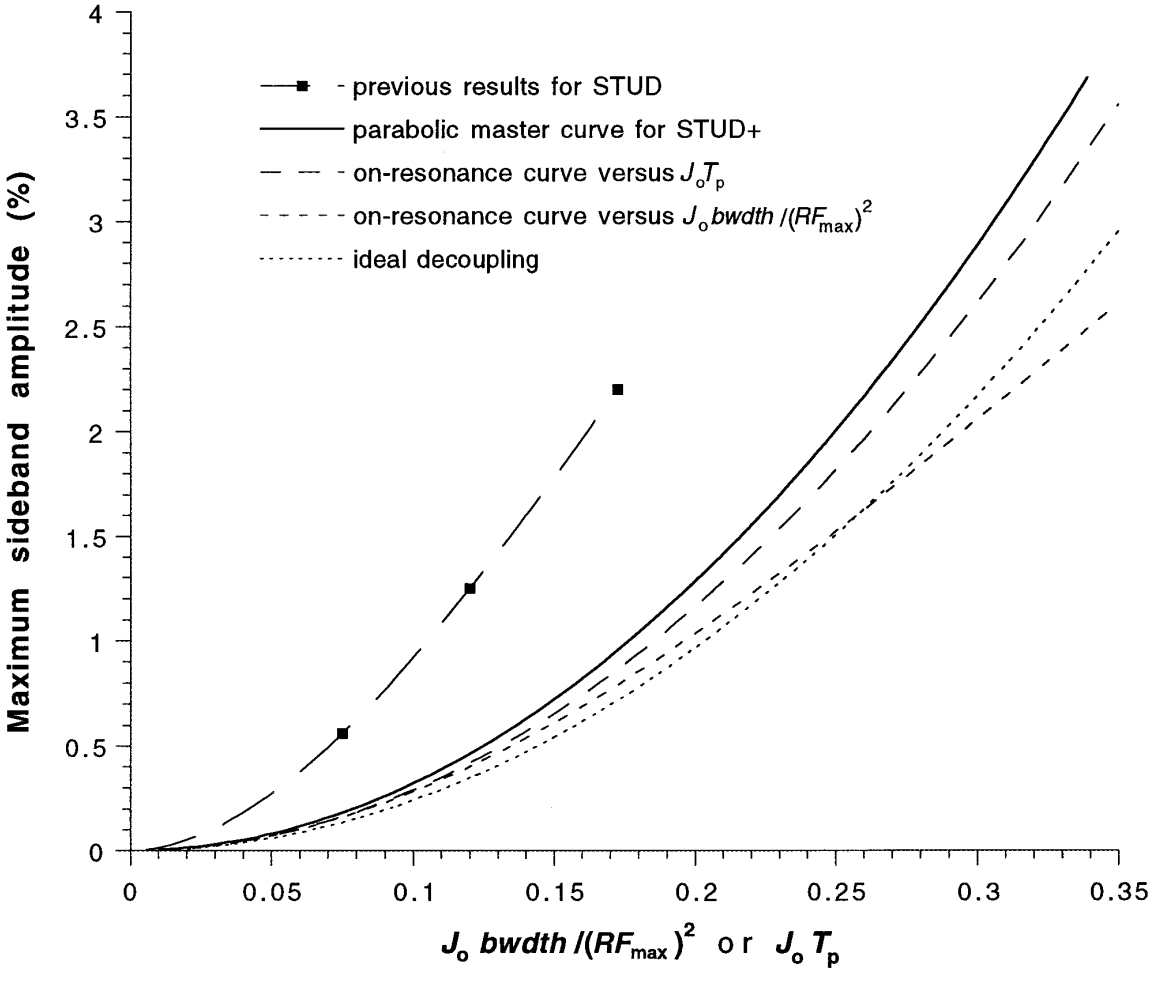

FIG. 9. Various plots of *MSB* versus J_oT_p or $J_ob_{/RF^2}$. The previous results for STUD are minimum *MSB* levels taken from Fig. 3a of Ref. (*2*), illustrating the improvement in decoupling performance using STUD+. The master curve for STUD+ is the alternative parabolic fit through the origin from Fig. 8. The on-resonance curve versus J_oT_p corresponds to Eq. [5], and the same data plotted versus $J_ob_{/RF^2}$ have been converted using Eq. [3]. The curve for ideal decoupling is given by Eq. [13]. The *x*-axes are dimensionless.

widths beyond 100 kHz will not diverge from the master curve much more than the $bwdth = 100$ kHz results.

The first step in utilizing these calibration curves is to choose a required effective bandwidth and an acceptable *MSB* level or, equivalently, a minimum *CB* level. The *MSB* values in Fig. 8 correspond to the edge of the effective bandwidth, and so most of the spectrum will be more efficiently decoupled. Also, most single-bond $^{13}C^{1}H$ coupling constants are around 150 Hz or less. So if an acceptable *MSB* is chosen to be 1.5% and $J_o \leq 150$ Hz, from Eq. [12] very few resonances will have a centerband amplitude less than 91% if the appropriate conditions calibrated in Figs. 6–9 are applied. Similarly, $MSB = 2.5$ or 2.5% leads to $CB \geq 86$ or 80%, respectively.

Accepting that $J_o \leq 150$ Hz for almost all ^{13}C resonances, and recognizing that within experimental error there are linear relations between MSB^{-1} and m_1 and m_2 (as described in the legend to Fig. 7), then from Eq. [9], *bwdth* can be determined from a chosen effective bandwidth, bw_{eff} as

$$bwdth = 1.3 + 0.8/MSB + (1.005 + 0.008/MSB)bw_{eff}. \quad [14]$$

T_p ($= b_{/RF^2}$) can be determined from the master curve equation in the Fig. 8 legend, but for $MSB \geq 1\%$, Eq. [11] suffices so

$$T_p = (MSB/0.72)^{0.5}. \quad [15]$$

From Fig. 6 the truncation factor, β, can be extracted as

$$\beta = \text{sech}^{-1}[0.235/(1 + 0.16bwdth)], \quad [16]$$

and finally, calculating RF_{max} from $b_{/RF^2}$ with the variable truncation factor included,

$$RF_{max} = (\beta bwdth/5.3T_p)^{0.5}. \quad [17]$$

In these equations, the units of $bwdth$, bw_{eff}, and RF_{max} are in kHz; T_p is in ms; and MSB is in percent.

If an upper limit of 150 Hz for J_o is considered to be too low, then a small correction can be made to $bwdth$ by linear interpolation between Eq. [14] and an equivalent equation derived from Fig. 7 for $J_o = 223$ Hz yielding

$$bwdth = 0.6 + 5e^{-3}J_o + 0.8/MSB + (0.995 + 7e^{-5}J_o + 0.008/MSB)bw_{eff}. \quad [18]$$

In addition, the more general equation,

$$T_p = (MSB/32)^{0.5}/J_o, \quad [19]$$

should be used in place of Eq. [15] (the units of T_p are changed back to seconds).

Thus all of the input parameters RF_{max}, β, T_p, and $bwdth$, for the sech/tanh pulse in STUD+ decoupling, as described in Eqs. [1] and [2], can be expressed in terms of chosen values of MSB, bw_{eff}, and J_o.

CONCLUSIONS

The major findings of this detailed study of the variables governing STUD+ broadband decoupling under the most efficient conditions are displayed in Fig. 8—master calibration curves for the centerband (CB), and for the maximum sideband amplitude (MSB), as determined by the four most critical experimental parameters: the maximum amplitude of the RF field, RF_{max}; the length of the sech/tanh pulse, T_p; the extent of the frequency sweep, $bwdth$; and the coupling constant, J_o. Less critical parameters (the truncation factor, β, and the effective decoupled bandwidth, bw_{eff}), which become more important as bandwidths are decreased, are calibrated in Figs. 6 and 7. These three figures will be most useful for ^{13}C decoupling, covering the range of one-bond $^{13}C^{1}H$ coupling constants from 125 to 225 Hz, and decoupled bandwidths of 7 to 100 kHz, with a bandwidth of 100 kHz being the requirement for a 2-GHz spectrometer.

It is straightforward to apply these calibration curves and their associated formulae. Determination of the most efficient conditions for broadband decoupling, in terms of minimizing the average RF power deposition in the sample, first requires the user to choose bw_{eff} for a particular decoupling application and either an acceptable minimum CB or an acceptable MSB. A chosen minimum CB can be converted to MSB via Eq. [12] and then all other parameters are given by Eqs. [14]–[17]. Alternatively, if an upper limit of 150 Hz for J_o is considered to be too low, Eqs. [18] and [19] can replace [14] and [15]. Even though the dependence on the most critical parameters can be summarized in one figure, this series of equations is required for accurate calibration of efficient decoupling. However, on an NMR spectrometer it is straightforward to combine all these equations in one computer macro which generates the entire STUD+ waveform based on user inputs of just MSB (or minimum CB), bw_{eff}, and maximum J_o.

While the coefficients in Eqs. [12], and [14]–[19], have all been determined by experiment, the form of these equations can be inferred from theoretical considerations and further support was obtained from computer simulations. In particular, via the expression $0.25[1 - \cos(\pi \bar{J} T_p/2)]$, which is half the amplitude of the S-spin FID modulation during the first decoupling pulse, the recent vector model of adiabatic decoupling in the high power limit (*3*) predicts CB decreases linearly as a function of increasing MSB, and it predicts a simple parabolic relationship between maximum sideband amplitude and the product J_oT_p. The relationships between $bwdth$, bw_{eff}, and β can be demonstrated by calculation of the inversion profile for a single pulse. Indeed, the only relation encompassed by these equations which does not have direct theoretical support is that between T_p and $b_{/RF^2}$ (i.e., $bwdth/(RF_{max})^2$), and even this is suggested by the basic equation that defines adherence to the adiabatic condition, as shown in (*2*). Considering the agreement between theory and the large number of experiments, we expect that we have determined true efficiency maxima for STUD+ and have not overlooked more efficient decoupling by some untried combination of these parameters.

The vector model also demonstrates that even if each adiabatic pulse in the decoupling scheme is ideal, cycling sidebands will still be generated (*3*). This allowed us to show in Fig. 9 that only a small percentage increase in efficiency was still theoretically possible in comparison to the large gain in going from STUD to STUD+. However, taking STUD+ as the new base level, if we consider a given MSB value, the theoretical performance limit for ideal decoupling is still 25% more efficient in terms of average RF power than can be achieved using the off-resonance set of calibration equations developed here, or 17% more efficient than can be obtained on resonance. So, a further improvement of, say, 10% in the performance of STUD+ might be considered possible and worthwhile. Furthermore, we have noted that this scope for improvement does not include any advantage that might be made in favourably changing the relationship between T_p and $b_{/RF^2}$. However, further overall gains of the order of 10% may be difficult to achieve by an approach that is primarily experimental as in this work, since the small improvements in decoupling performance that might comprise an overall 10% improvement will not be obvious relative to experimental error. Such advances might be better approached through theoretical simulations. The knowledge obtained from the present study can be used as a guide or basis for such simulations. For example, calculations of MSB levels for different phase cycles can be compared with

the estimate given by the expression for ideal decoupling, $0.25[1 - \cos(\pi \bar{J} T_p/2)]$, as a performance indicator. Another approach would be to attempt to improve the squareness of the profiles for decoupling over small to moderate bandwidths (decrease the m_1 values of Fig. 7), by changing the form of the adiabatic pulse, and it should be sufficient to investigate the inversion profiles of single pulses for this purpose. We also expect that characterization of bw_{eff} by exhaustive computer simulations, rather than the experimental approach used here, should improve efficiency by about 5%.

We now propose that there are three major requirements for efficient adiabatic decoupling. First, the key to recent developments has been improvements in the phase cycle. When composite-pulse decoupling was introduced, it was noted (*17*) in regard to adiabatic decoupling, "Unfortunately with this (phase) cycle it is difficult to meet the adiabatic conditions and still complete a full (phase) cycle in a short time compared with $1/(2\pi J)$ sec." From the vector model (*3*), this work, and other recent studies, we now know that the requirement is that the length of the adiabatic inversion pulse T_p, not the phase cycle or one of the constituent subcycles, should satisfy the relation $\pi J\, T_p/2 \ll 1$, since this limits the size of the $1/T_p$ sideband which dominates under ideal adiabatic conditions. A good phase cycle is then required to correct for poor inversions at lower RF power. The four-phase M4 cycle, developed theoretically and extended in the MLEV cycles as used in composite-pulse decoupling (*17*), was also used for CHIRP (*17, 18*), the first application of adiabatic decoupling. Progressive improvements in decoupling performance were demonstrated in DAP-16 (*15*) using the MLEV16 cycle (*7*), in STUD (*1*) with the M4P5 cycle (*13*), and then additional useful cycles resulted from a new algorithm (*4*) combined with cycle concatenation and inclusion of the P9 cycle (*12, 14*), yielding STUD+. All the competitive schemes listed in Ref. (*4*) are concatenations of the singly nested cycles, M4P5, M4P9, and P5P9, but doubly nesting the cycles as in P5M4P9 is not effective. Any further significant improvement in phase cycling would thus seem to require a new competitive single cycle to add to M4, P5, and P9, if that is possible.

The second major requirement is a good adiabatic inversion pulse. The sech/tanh pulse (*5*) is more than a decade older than a recently discovered family of pulses which are characterized by the property that the time derivative of the frequency modulation function is proportional to the square of the amplitude modulation function (*19, 20*) (making the minimum adiabaticity of the pulse relatively insensitive to resonance offset). Tannús and Garwood (*20*) demonstrated that members of this family of pulses have the same inversion efficiency at the center of the inversion bandwidth at the same average RF power and the same *bwdth* value. While this indicates that they will provide equivalent decoupling performance on resonance, the outstanding decoupling performance of the sech/tanh pulse is directly related to b_{eff} being very close to 100% of *bwdth*, as has been demonstrated here and elsewhere. Therefore none of these new pulses can be expected to have a significant improvement in this area. In addition, the sech/tanh pulse is already a member of this family, so there is no further improvement the method of Refs. (*19, 20*) can make to the sech/tanh pulse. However, we have obtained improved inversion profiles by modifying the sech/tanh waveforms to make the minimum adiabatic factor for the pulse exactly constant over a large range of resonance offsets. But the complexity of the procedure requires a numerically designed pulse, and the 5–10% potential improvement is counterbalanced by the simplicity of implementing the original sech/tanh waveform with computer macros.

The third major requirement is to maximize efficiency with respect to the ideal performance limits discussed here and in Ref. (*3*) by determining the coefficients of the simple linear and parabolic relationships between the relevant decoupling parameters which are summarized in Eqs. [12] and [14]–[19] for STUD+ decoupling. We expect this procedure will be general for any good combination of adiabatic inversion pulse and phase cycle. These formulae are concerned with single decoupled NMR transients and so both minimize sideband amplitudes and maximize centerband amplitudes, which is not possible via multi-transient methods.

REFERENCES

1. M. R. Bendall, *J. Magn. Reson. A* **112,** 126 (1995).
2. M. R. Bendall and T. E. Skinner, *J. Magn. Reson. A* **120,** 77 (1996).
3. T. E. Skinner and M. R. Bendall, *J. Magn. Reson.,* **134,** 315 (1998).
4. T. E. Skinner and M. R. Bendall, *J. Magn. Reson.* **124,** 474 (1997).
5. M. S. Silver, R. J. Joseph, and D. I. Hoult, *J. Magn. Reson.* **59,** 347 (1984).
6. M. R. Bendall and T. E. Skinner, *J. Magn. Reson.* **129,** 30 (1997).
7. M. H. Levitt, R. Freeman, and T. Frenkiel, *J. Magn. Reson.* **47,** 328 (1982); A. J. Shaka, J. Keeler, and R. Freeman, *J. Magn. Reson.* **53,** 313 (1983).
8. M. R. Bendall, *J. Magn. Reson. A* **116,** 46 (1995).
9. Ē. Kupče and R. Freeman, *J. Magn. Reson. A* **115,** 273 (1995).
10. T. E. Skinner and M. R. Bendall, *J. Magn. Reson. A* **123,** 111 (1996).
11. R. Tycko and A. Pines, *Chem. Phys. Lett.* **111,** 462 (1984).
12. R. Tycko, A. Pines, and J. Guckenheimer, *Phys. Rev. Lett.* **56,** 1905 (1986).
13. T. Fujiwara and K. Nagayama, *J. Magn. Reson.* **77,** 53 (1988).
14. T.-L. Hwang, A. Tannús, M. Garwood, and P. C. M. Van Zijl, Abstracts of the 37th ENC, Asilomar, California, March 1996; T.-L. Hwang, M. Garwood, A. Tannús, and P. C. M. Van Zijl, *J. Magn. Reson. A* **121,** 221 (1996).
15. Z. Starčuk, Jr., K. Bartušek, and Z. Starčuk, *J. Magn. Reson. A* **107,** 24 (1994).
16. J. S. Waugh, *J. Magn. Reson.* **50,** 30 (1982).
17. M. H. Levitt and R. Freeman, *J. Magn. Reson.* **43,** 502 (1981).
18. V. J. Basus, P. D. Ellis, H. D. W. Hill, and J. S. Waugh, *J. Magn. Reson.* **35,** 19 (1979).
19. Ē. Kupče and R. Freeman, *J. Magn. Reson. A* **118,** 299 (1996).
20. A. Tannús and M. Garwood, *J. Magn. Reson. A* **120,** 133 (1996).